3D bioprinted colorectal co-culture model to explore nanoparticles targeting and stimuli responsive treatments against cancer

Materials & Design 257 (2025) 114478

Contents lists available at ScienceDirect

Materials & Design

journal homepage: www.elsevier.com/locate/matdes

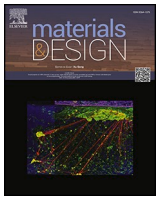

3D bioprinted colorectal co-culture model to explore nanoparticles targeting and stimuli responsive treatments against cancer

Giorgia Savino [a], Giada Rosso [a], Maria D'Aloia [a,b], Ignazio Roppolo [a], Valentina Cauda [a,*]

[a] Department of Applied Science and Technology, Politecnico di Torino, Corso Duca degli Abruzzi 24, 10129 Turin Italy
[b] Department of Chemistry, Biology and Biotechnology, University of Perugia, Via Elce di Sotto 8, 06123 Perugia, Italy

ARTICLE INFO

Keywords:
3D bioprinting
Colorectal cancer
Lipid bilayers
Biomimetic ZnO nanoparticles
Peptide-mediated targeting
Acoustic pressure waves
Remotely-controlled treatment

ABSTRACT

Colorectal cancer (CRC) is a major global health challenge and a leading cause of cancer-related deaths, with prevalence expected to double by 2040. Traditional treatments face significant limitations, including resistance, recurrence, and toxicity. Nanomedicine offers promising alternatives through advanced nanoparticles, such as drug-delivering or stimulus-activated systems, but clinical translation remains challenging. Current animal models often fail to accurately predict human outcomes, highlighting the need for better testing platforms.

Three-dimensional (3D) colorectal cancer models provide an ethical, cost-effective alternative to animal studies, mimicking human tumor microenvironments with high fidelity. Here we bioprinted 3D hollow conduits to develop a CRC model, co-culturing healthy and cancer cells, enabling controlled and rapid testing of therapies with improved reproducibility. Unlike 2D cultures or animal models, the proposed 3D bioprinted model provides insights into tumor-specific responses under therapeutic treatments and bio-stability over long time span. It serves as in vitro biological twin of CRC to test innovative nanomedicine treatments, aiming to bridge preclinical and clinical research.

We create hybrid biomimetic nanoparticles designed to target CRC tumors while sparing healthy tissue. These nanoparticles are activated by acoustic waves to induce cancer-specific cell death. Their safety and efficacy are tested in the bioprinted 3D models, advancing personalized CRC treatments.

1. Introduction

Colorectal cancer (CRC) is a major global health concern, ranking as the third most common malignant neoplasm and the second leading cause of cancer-related death worldwide. In 2020, an estimated 1.93 million new cases were reported globally, accounting for approximately 10 % of all cancer-related mortality in Western countries [1]. The high lethality associated with CRC is expected to persist in the coming decades, with global prevalence anticipated to double by 2040 [2].

Traditionally, surgical intervention and postoperative adjuvant chemotherapy have constituted the primary therapeutic treatments against this malignancy [3,4]. However, chemotherapy drugs present numerous side effects and limitations, as acquired resistance, low tumor-specific selectivity and low biocompatibility. Furthermore, these therapies are frequently ineffective to prevent the recurrence of localized CRC or the development of metastasis, happening in almost 40 % of cases, and they are nearly ineffective in advanced CRC cases. Therefore, recent years have seen an unprecedented shift in research towards novel approaches such as targeted therapy and nanomedicine. These new methods aim to enhance treatment effectiveness and achieve more precise personalized therapy, increasing compliance with patient's needs [5]. In this scenario, nanoparticles (NPs) carrying chemotherapeutic compounds or even advanced NPs which can act as drugs upon activation through an exogenous stimulation (such as light, magnetic field, or ultrasound) are under consideration [6,7].

Despite the integration of several nano-pharmaceuticals into clinical practice, numerous nanomedicine-based approaches remain under evaluation. Actually, fewer than 10 % of novel anticancer drug candidates in clinical trials ultimately receive FDA approval [8]. The slow pace of drug and nano-pharmaceutical approvals, coupled with the use of simplistic preclinical models, compromises the clinical efficacy of these emerging cancer treatment agents during trials [9]. The complexity of the intestine, characterized by its heterogeneity with numerous functions and unique dynamic conditions, presents a substantial challenge for accurate reproduction in ongoing research [10]. This complexity further complicates the development and clinical

* Corresponding author.
E-mail address: valentina.cauda@polito.it (V. Cauda).

https://doi.org/10.1016/j.matdes.2025.114478
Received 8 February 2025; Received in revised form 30 June 2025; Accepted 28 July 2025
Available online 28 July 2025

evaluation of novel therapeutic strategies.

Over the past years, despite being the gold standard, animal models and *in vivo* experiments have demonstrated poor performance in terms of predicting future therapeutic responses in human clinical trials [11]. Besides well-known issues such as being labor-intensive, expensive, lacking in repeatability and posing ethical concerns [12], murine models do not accurately reflect the full pathophysiology of CRC [13]. While some murine models are valuable tools for understanding the development and progression of CRC, they simplify the disease and do not account for the multifactorial nature of the tumor [14]. Consequently, these considerations have led the scientists to pursue a progressive conceptual construction of *ideal* biomimetic organ models in agreement with the 3Rs principle (Reduce, Refine, Replace) [15].

In vitro three-dimensional (3D) intestine models can offer simple, cost-effective, and standardized tools to reproduce complex intestinal processes that are challenging to control *in vivo* [10]. The ideal in vitro CRC model should replicate all the essential features and functionalities of its biological counterpart yet being an in vitro biological twin. CRC pathophysiology is indeed characterized by adenomatous polyps and adenocarcinoma, epithelial tumors of the large intestine and the most common and clinically significant of intestinal neoplasms. To accurately replicate these colorectal neoplasms, essential components of 3D CRC model should include: human-derived cells from diverse regions of the colon; a 3D structure with properties mimicking the native environment; biochemical, physical, and structural stimuli; a fluidic system ensuring adequate oxygenation and nutrient supply, and a biochemical environment that includes interaction between the epithelium, immune system, and colon microbiota [10,16].

Various tissue-engineering, scalable and cost-effective techniques, including 3D bioprinting have been implemented as potential approaches to fabricate tissue constructs by layer stacking of biomaterial and living cells [17].

Coaxial bioprinting has been employed to develop tubular channels encapsulating cells, mimicking the natural blood vascular system. Nevertheless, the same methods can be exploited in the biofabrication of circumferentially multilayered tubular tissues with cellular heterogeneity, such as the colon [18]. In this regard, in 2013 Yu *et al.* developed an innovative method to print vessel-like structures comprising cell-encapsulated structures obtained through the co-extrusion of sodium alginate and calcium chloride solutions. A first system was presented after describing the investigation of how different process parameters affect cell viability during and after the bioprinting procedure [19]. Following this work, novel studies were conducted regarding specifically the bioink blend. In 2016, Jia *et al.* improved the biological characteristics of the bioink introducing materials to support the spreading and proliferation of the cell encapsulated in the bioprinted constructs. In particular, the bioink was based on gelatin methacryloyl (GelMA), sodium alginate and 4-arm poly(ethylene glycol)-tetra-acrylate (PEGTA). The introduction of a PEG-derived component displayed favorable biological and mechanical properties that supported the spreading and proliferation of the encapsulated cells and enabled the maintenance of a stable conduit [20]. To achieve more reliable results, a further improvement was introduced in a later article were Pi *et al.* studied a customized blend bioink with improved rheological properties. It was formulated by mixing a solution of GelMA, sodium alginate and eight-arm poly(ethylene glycol) acrylate with tripentaerythiritol core (PEGOA). The bioink blend showed not only to possess the suitable rheological properties but also to guarantee the maintenance of a high cell viability and structural integrity of the conduits [18,21]. In their most recent articles, the group of Pi presented an even more reliable microfluidic bioprinting system characterized by a double-network (DN) hydrogel bioink system with high biocompatibility and better mechanical properties. The bioink prepolymer was composed of sodium alginate and gelatin subsequently crosslinked by calcium chloride and microbial transglutaminase (mTG). After the removal of the physical network of the DN hydrogel by EDTA, the gelatin network would maintain the material integrity, assuring both favorable biological properties and mechanical stability [22].

In this work, we present a bioink formulation based on alginate and gelatin for coaxial 3D bioprinting, adopting the benefit of dual crosslinking with mTG and calcium chloride ($CaCl_2$). We aim to produce a 3D colon model specifically designed to incorporate healthy cells in the tube's walls and mimic the development of adenocarcinoma in the colon lumen.

We utilize this model as an advanced preclinical platform to study the biodistribution, safety and bioavailability of smart NPs in this 3D volume, identifying also the advantage of targeting moieties in guiding the NPs towards the tumor masses, while sparing the healthy tissue. In particular, a targeting peptide (YSA), specifically designed to recognize the Ephrin A2 protein overexpressed in certain CRC masses, has been adopted as a proof of the targeting concept [23].

Exploiting the advantages of such 3D colon structure, we further explore the effects of a novel stimuli-responsive therapy to activate the therapeutic effect of the administered NPs. In particular, we adopt the use of acoustic pressure waves, such as continuous low-intensity ultrasound and high-pressure shockwaves. These stimulations propagate easily in liquid or 3D volumes, and in humans are able to reach deeply-located tissues and display harmless effects in the human body [24]. Recent approaches like microbubble contrasted echography and sonodynamic therapy have shown both the diagnostic and the therapeutic powers of these acoustic pressure waves *in vivo* and in humans [24].

In this work, we present an optimized coaxially bioprinted colon model where normal cells are directly extruded into the tubular walls and cancer cells are seeded inside the model, resulting in the generation of a 3D co-culture. The innovation of this work relies in the 3D in-vitro hollow tube model created through coaxial bioprinting, using a custom-designed bioink and co-extruded with healthy and cancerous living cells. The model maintains cell viability for over 13 days, ensuring long-term stability and effectively mimicking cancer tissue. As far as we know, such model was not yet proposed in the literature and the reported examples above from the state-of-the-art refers to models for cardiovascular applications, and none of them is intended for long-term studies. Furthermore, we adopted the use of nanoparticles-mediated acoustic pressure waves to evaluate the possible therapeutic efficacy of such a combined approach in a complex 3D environment. (Fig. 1). We thus simulate in a 3D biological twin of CRC the possible therapeutic effects of a targeted and stimuli-responsive nanomedicine therapy, particularly addressing the produced tumor masses, while minimizing damage to health tissues of the tube. To our knowledge, this is the first demonstration of this nanomedicine-based and stimuli-responsive approach applied to a 3D CRC model, showing promises for future clinical applications.

2. Material and methods

2.1. Preparation of the Bioink

To prepare the components of the bioink, gelatin from porcine skin (type-A, 300 bloom) and alginic acid sodium salt from brown algae (medium-viscosity) were dissolved in bidistilled water (bdH_2O), physiological solution at 0.9 % wt of sodium chloride or Stable Cell MEM cell culture media to make an initial 30 % (w/v) and 4 % (w/v) solution, respectively. To analyze the printability of the structures, different concentrations of the components were tested: i) 8 %, 10 %, or 15 % gelatin and 1 % alginate in bdH_2O; ii) 15 % gelatin and 1 % alginate in physiological solution; iii) 15 % gelatin and 1 % alginate in cell culture medium, iv) 8 % gelatin and 2 % alginate in cell culture medium, v) 11 % gelatin and 2.5 % or 3 % alginate in cell culture medium. Solutions were stirred at 50 °C until homogeneity was reached. Similarly for the crosslinking solution, $CaCl_2$ was dissolved in 4 % (w/v) bdH_2O, physiological solution or Stable Cell MEM cell culture. Likewise, stock solutions of 10 % (w/v) mTG, purchased from Ajiomoto North America. Inc

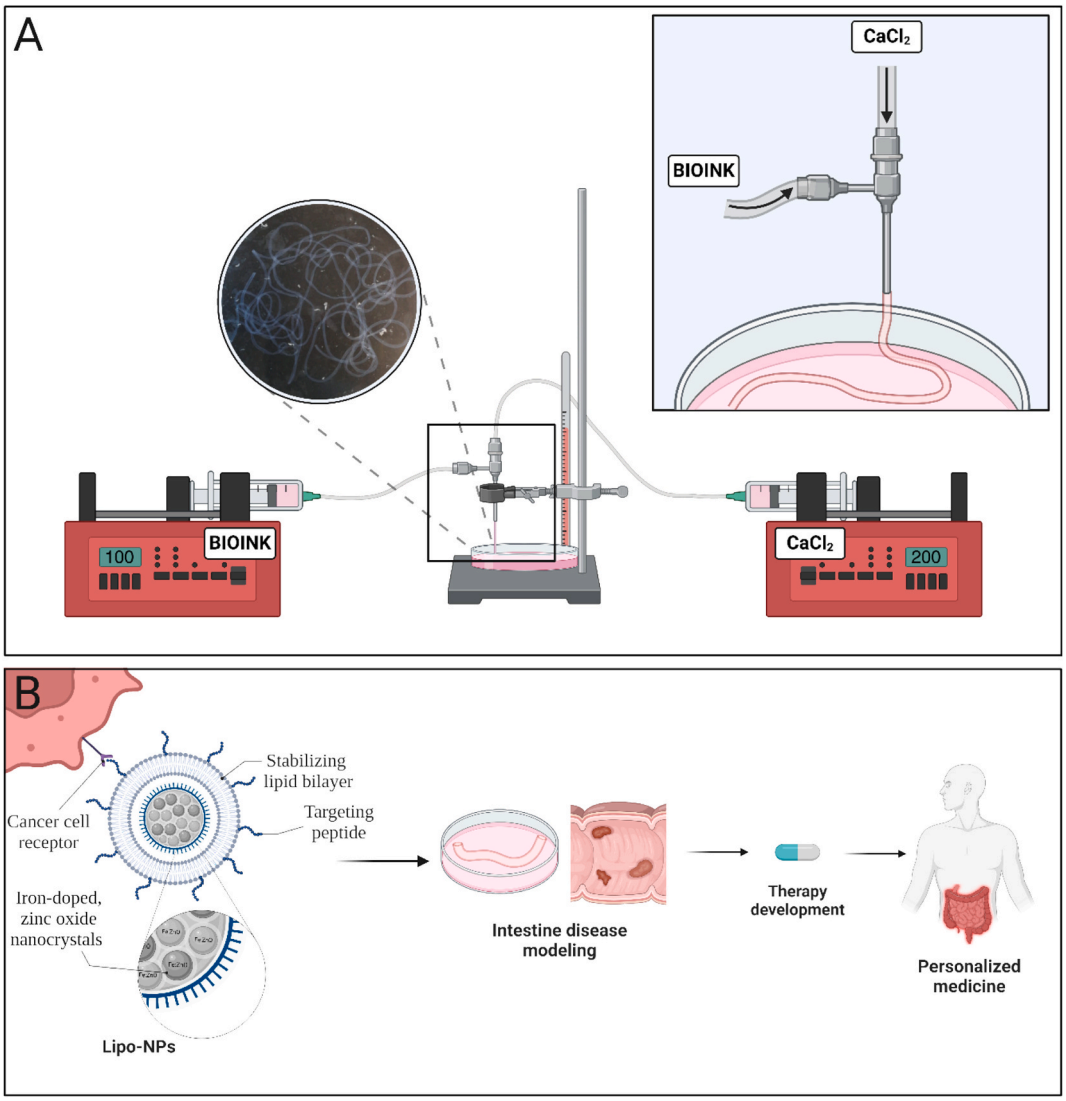

Fig. 1. Scheme of the experimental set up and proposed stimuli-responsive treatment (**A**) Schematics showing the experimental setting of the printing system and the coaxial nozzle assembly for the microfluidic extrusion of the (bio)printed hollow conduits (**B**) Design of the biomimetic nanoparticles composed of zinc oxide ZnO nanocrystals (ZnO NCs) coated with a self-assembling lipid formulation (L-ZnO), subsequently conjugated with a targeting peptide (YSA) specifically designed to recognize the Ephrin A2 expression in CRC, then incubated with the 3D intestine tumor models.

(Fort Lee, NJ, USA), were prepared. Stock solutions of $CaCl_2$ and mTG were further filtered using Stericup TM Quick Release-HV Sterile Vacuum Filtration system. All solutions were stored at 4 °C until use.

2.2. Bioprinting setup

The bioprinting system comprised two microfluidic syringe pumps (Model DUAL-NE-1000, KF Technology), loaded with two syringes containing the hydrogel precursor and 2 % $CaCl_2$ solution (Fig. 1A). These syringes were connected to the external and internal channels of a commercial coaxial needle with 17G and 23G nozzles, respectively. The extrusion speeds were set to 100–250 μL/min for the bioink and 200–500 μL/min for the $CaCl_2$ solution, depending on the concentration employed. The entire process was performed under sterile conditions. Before bioprinting, all equipment was cleaned with 70 % ethanol and subjected to UV radiation for 30 min for sterilization. The coaxial needle was sterilized by rinsing with sodium hypochlorite, phosphate buffered saline (PBS) and 99 % ethanol solution. To maintain the bioink at its optimal viscosity for printing, a heater was used to keep the temperature around 28–30 °C.

2.3. Extrusion of acellular hollow tube

To obtain acellular conduits, the bioink was heated to 45 °C and centrifuged at 500 g for 2 min to remove any bubbles. Subsequently, the bioink and a 2 % $CaCl_2$ solution were transferred respectively into a 10 mL and 20 mL syringe and connected to the inlets of the outer and the core channel of the coaxial nozzle using silicon tubes. The $CaCl_2$ solution and the bioink were placed on separate syringe pumps and extruded simultaneously. The bioprinted hollow tubes were collected in a 150 mm Petri dish filled with 1 % $CaCl_2$ solution. To facilitate the stabilization of the alginate hydrogel, the extruded conduits were gently submerged under the $CaCl_2$ solution surface using a swab, pre-soaked in the same solution. As an alternative, a spray of $CaCl_2$ solution was used to crosslink the outer surface of the printed tubes during the extrusion. At the end of the process, and before incubation at 37 °C in an atmosphere of 5 % CO_2, the bath solution was replaced with a 2 % $CaCl_2$ and 2 % mTG solution to further crosslink the conduits overnight.

2.4. Rheology measurements

Rheological measurements were performed using ad Anton PAAR

Modular Compact Rheometer (Physica MCR 302, Graz, Austria) in parallel-plate mode (25 mm diameter), equipped with a Peltier cooling system (H-PTD200).

Firstly, viscosities of the bioinks were evaluated with continuous flow measurements performed with a range of shear rate from 0.001 to 1000 s^{-1}. Gap between plates was set to 0.5 mm and temperature was set to 37 °C in all tests. Outlier values have been neglected.

Secondly, to evaluate the change in viscosity with temperature, temperature ramp test was conducted on the optimal bioink with a rate of 2 °C/min, from 20 to 44 °C, maintaining a gap of 0.5 mm and a constant shear rate of 100 s^{-1}.

Then, frequency sweep tests were conducted on the optimal bioink to study variations in G' and G'' moduli in the range of 0.1 to 100 Hz, with a constant amplitude of 1 %. Gap was kept at 0.5 mm and temperature at 37 °C.

Amplitude sweep tests were performed on crosslinked bioink disks (thickness of 1.8–2.4 mm, diameter of 25 mm). Gap was set accordingly to the thickness of the disks, and temperature was kept at 37 °C. Amplitude sweep tests were performed in the range of 1 to 1000 % strain, with a constant frequency of 1 Hz. In addition, amplitude burst in time strain was performed as a succession of three steps with constant amplitude equal to 50 %, 1000 % and 50 % in the three steps, respectively. Frequency was constant in the three steps and equal to 1 Hz.

2.5. Mechanical characterization

Tensile test was conducted using a Z3 tensile tester (AML Instruments) with a 500 N load cell equipped with tensile grippers. The data processed using THSSD software. Tests were conducted at a rate of 10 mm/min on 8 dumbbell-shaped specimens (51.8 ± 2.3 cm useful length, 11.4 ± 0.8 cm width at center and 3.5 ± 0.6 cm thickness). Specimens were fabricated by crosslinking the bioink solution in a 2 % $CaCl_2$ bath for 15 min, followed by immersion in a 2 % mTG solution overnight. After crosslinking, the specimens were cut into dumbbell shapes using a shaped template.

Specimens were brought to failure and properties such as elastic modulus, stress at break, and elongation at break were evaluated as the average of values obtained on 8 specimens.

2.6. Cell cultures

The human colorectal adenocarcinoma HT-29 cell line (product HTB-38 from ATCC) was grown in 25 or 75 cm^2 treated flasks with RPMI 1640 (Sigma) and supplemented with 10 % heat inactivated fetal bovine serum (FBS, Sigma) and 1 % of 100 μg/mL of streptomycin/100 units/mL of penicillin (P/S, Sigma-Aldrich).

The human cell line CCD-18Co (product CRL-1459 from ATCC) from colon tissue was instead employed as healthy control. It was cultured in Stable Cell MEM (Sigma) supplemented with 10 % FBS, 1 % P/S, 1 % MEM, 1 % L-Glut and 1 % sodium pyruvate.

All cells were maintained in a humidified incubator at 37 °C with an atmosphere of 5 % CO_2. Both cell lines grow adherent to the flask and form dense cell colonies, therefore, before the encapsulation or seeding process, cells were trypsinized.

2.7. Extrusion of cell-laden hollow tube

To obtain cell-laden tubular conduits (hollow bioprinted tubes where cells are embedded in the bioink) the bioink components, $CaCl_2$ and mTG solution were dissolved in Stable Cell MEM cell culture media. Before the bioprinting process, CCD-18Co cells were resuspended in the hydrogel precursor solution at a concentration of 2 x 10^6 cells/mL. The solution was subsequently transferred to a 10 mL syringe for microfluidic bioprinting. The printing set up and the extrusion parameters for the cell-laden conduits were maintained unvaried from those used for printing acellular hollow tube. For this process, the bath solution was replaced exclusively with a 2 % mTG solution to further crosslink the conduits overnight, prior to incubation at 37 °C in 5 % CO_2.

2.8. Cell seeding in hollow tube

The process of cell seeding was done the day after the extrusion of the hollow tubes, always under sterile conditions. The hollow conduits were cut in segments of 5–6 cm in length. HT-29 cells were resuspended at concentration of 1 x 10^7 cells/mL in RPMI 1640 cell culture. The HT-29 suspension was loaded into a 1 mL syringe and injected into the lumen of the bioprinted tubes using a sterile hypodermic 26G needle. After cell seeding, the bioprinted conduits were transferred to a 24-well plate for the following administration of the US treatment or to a 6-well plate, where a PDMS holder was employed to maintain their orientation for subsequent shockwave therapy (SWT) with a linear transducer. In each well a mixed medium prepared by combining Stable Cell MEM and RPMI 1640 in a 1:1 ratio was added and changed every 2 days. The co-culture was incubated at 37 °C in an atmosphere of 5 % CO_2 until cells formed a compact structure.

2.9. Optical microscopy

After bioprinting and cell seeding, bright-field inverted optical microscopy was performed to verify the model's shape and integrity, assess cell seeding accuracy and monitor cellular growth and development. For all the analysis a spinning disk fluorescence microscope (Ti2 Nikon equipped with Crest V2 Large FOV LED source) and a high-resolution camera (Zyla 4,2 Plus, 4098x3264 pixel, Andor Technology) were employed. The images were taken with a 4X PlanAPO objective (NA = 0.20).

2.10. NPs Synthesis

Iron-doped (6 at.%) zinc oxide nanocrystals (ZnO NCs) were synthetized following a procedure already established in previous works of our group [25]. Briefly, 526 mg zinc acetate di-hydrate ($Zn(CH_3COO)_2{\cdot}2H_2O$, Sigma-Aldrich) and 58 mg of ferric nitrate hexahydrate ($Fe(NO_3)_3{\cdot}9H_2O$, HiMedia) were dissolved in 40 mL of absolute ethanol (99 %, Sigma-Aldrich) as precursors for iron doping. The dissolved salts were transferred to a round bottom flask, and the solution was heated to 70 °C and stirred until the complete dissolution of zinc and iron precursors. Additionally, 140 μL of oleic acid capping agent (≥99 %, Sigma-Aldrich) and 1 mL of bidistilled water (obtained from a Direct Q3 system, Millipore) were added. To initiate particle condensation, a solution containing 1.044 g of tetramethylammonium hydroxide pentahydrate (TMAH, 98.5 %, Sigma-Aldrich), 10 mL of ethanol and 1.052 mL of water was rapidly added to the precursors under continuous stirring at 70 °C. The ZnO NC suspension was collected after 10 min, and 40 mL of ice-cooled ethanol were added to the solution to inhibit the reaction. The resulting colloidal solution was centrifuged at 8000 g for 10 min and washed three times with fresh ethanol. Subsequently, the ZnO NCs were functionalized with amino propyl groups for dye attachment in in vitro applications. Specifically, ZnO NCs were suspended in ethanol at a concentration of 2.5 mg/mL, heated to 70 °C with moderate stirring under reflux conditions in a nitrogen atmosphere. Finally, 8.6 μL of (3-Aminopropyl) trimethoxysilane (APTMS, Sigma-Aldrich), equal to 10 mol% of ZnO, were added and the ZnO NCs dispersion was stirred under an inert atmosphere for 6 h. After the reaction, the dispersion was centrifuged at 12,000 g for 20 min, the supernatant discarded, and the particles were washed twice and resuspended in 10 mL of ethanol.

2.11. NPs coating with lipid bilayer and conjugation with targeting peptide

A lipid-coating was provided to the ZnO NCs, following a previously

developed protocol [26]. The stable coating consisted in a solvent exchange method which exploits an electrostatic interaction between the ZnO NCs and the lipid mixture. In particular, the mixture was constituted by the anionic phospholipid DOPA (18:1 PA, 1,2-dioleoyl-*sn*-glycero-3-phosphate sodium salt, chloroform solution), the neutral charged phospholipid DOPC (18:1 (Δ9-Cis) PC (DOPC), 1,2-dioleoyl-*sn*-glycero-3-phosphocholine, chloroform solution), PEGylated lipids with functional amine and maleimide groups (respectively DSPE-PEG(2000) Amine (1,2-distearoyl-*sn*-glycero-3-phosphoethanolamine-N-[amino (polyethylene glycol)-2000] (ammonium salt)) and DSPE-PEG(2000) Maleimide (1,2-distearoyl-*sn*-glycero-3-phosphoethanolamine-N-[maleimide(polyethylene glycol)-2000] (ammonium salt)), all purchased from Avanti Polar Lipids and cholesterol in chloroform solution, at a molar ratio of 50:10:1.5:38.5. In addition, a PEGylated phospholipid was used to anchor the ephrin-mimetic peptide YSA, specifically targeting the EphrinA2 (EphA2) receptor [27], present in CRC cell line (The human protein Atlas) and previously confirmed by us in the HT-29 CRC cell line [23]. A targeting peptide-lipid was achieved by adding 0.3 % molar of the DSPE-PEG (2000)-Maleimide (1,2-distearoyl-*sn*-glycero-3-phosphoethanolamine-N-[maleimide(polyethylene glycol)-2000] (ammonium salt))) from Avanti Polar, precedingly conjugated with the aminoacidic sequence mixture YSAYPDSVPMMSC (prepared by BioFab Research srl, Rome, Italy), through the reaction of the maleimide group exposed by the PEGylated phospholipid and the cysteine contained in the peptide, as previously reported by *Rosso at al.* [23]. The peptide solution was prepared by adding DMF, reaching 50 mM peptide concentration and successively diluted with 0.1 M PBS (pH = 7.4), achieving 10 mM final concentration. The lipid solution is added to the obtained mixture following a 3:1 phospholipid:peptide molar ratio. The lipid coating of ZnO NCs with and without YSA-peptide was performed through the solvent exchange method in which the lipids and, where necessary, the YSA-conjugated DSPE-PEG were mixed and dried under vacuum at room temperature overnight. The following day the dried lipids were resuspended in an ethanol water solution (40 %vol. ethanol, 60 %vol. bdH_2O), achieving a final concentration of 3 mg/mL. The designed amount of ZnO NCs, collected from a stock solution kept in ethanol at 4 °C, was centrifugated at 14000 g for 10 min. Supernatant was discarded, and the lipid dispersion was added to the pellet, observing a NPs:lipids mass ratio of 2:1. After 3 min of sonication at 59 kHz in an ultrasound bath (Branson 3800 CPXH), bdH_2O was quickly added to generate the self-assembly of the lipids around the ZnO NCs. The final concentration of the obtained lipid coated (L-ZnO) or YSA-targeted (YSA-L-ZnO) ZnO NCs was set to 1 mg/ml and additional sonication of 5 min was applied to homogenize the sample.

2.12. NPs characterization

To evaluate the correct assembly of the nanoconstructs, the hydrodynamic radius and surface charge of the nanoparticles were investigated through Dynamic light scattering (DLS) and Z-potential analysis with a Zetasizer Nano ZS90 instrument (Malvern Panalytical, Malvern, UK). The measurement of each prepared suspension of uncoated, coated or targeted ZnO NCs (ZnO, L-ZnO and YSA-L-ZnO) were performed in bdH_2O dispersing NPs at a concentration of 100 μg/mL.

In order to qualitatively evaluate the binding of the YSA peptide in the YSA-L-ZnO nanoconstructs, a colocalization analysis through fluorescence microscopy was performed. Before the lipid coating, the ZnO core was labelled with ATTO 550-NHS ester (Thermofisher), by adding 2 μL of the dye (2 mg/mL in DMF) for each mg of ZnO. To let the reaction between the dye and the aminopropyl group (exposed by the NPs) take place, the NPs were resuspended in ethanol at a concentration of 1 mg/mL and stirred overnight in the dark. Successively, the unbound dye was eliminated through two cycles of centrifugation at 14,000 g for 10 min and substitution of the supernatant with fresh ethanol. The so obtained NPs, were then coated with a lipid mixture, containing a FITC-labelled YSA peptide (from Bio-Fab Research srl), following the usual procedure. The sample, after a 10^3-10^4 times dilution in water (to obtain the optimal concentration), was spotted on a glass slide and analyzed. Fluorescence microscopy images were acquired utilizing a spinning disk confocal microscopy (Ti2 Nikon equipped with a crest large FOV laser and a 100 × PlanAPO objective, NA = 1.30). A minimum of 10 images per sample were analyzed with the object count tool of the NIS software from Nikon.

2.13. Stimuli-responsive NPs treatment

The bioprinted conduits, with CCD-18Co cells embedded in the hydrogel wall and HT-29 cells inoculated in the lumen were incubated with the two different samples of nanoparticles: L-ZnO and YSA-L-ZnO NPs and then used for the stimuli responsive treatments with acoustic waves (see scheme in Fig. 2). In detail, after coaxial bioprinting with CCD-18Co-laden bioink at day 0 and HT-29 cell seeding at day 1, the bioprinted conduits were placed in a 24-wells or 6-wells plate for growth, respectively for the ultrasound and shock waves treatment. At least one empty well was left in each direction to avoid the influence of the acoustic treatment. Six days after the extrusion of the bioprinted models, each well was filled with 500 μL or 2 mL (respectively, for 24-well and 6-well plates) of mixed culture media, in which were precedingly dispersed 0 (control) or 200 μg/mL of L-ZnO or YSA-L-ZnO NPs. After 24 h of NPs incubation (i.e. at day 7), the 3D models were subjected to multiple acoustic wave treatments for three consecutive days, conducted with either ultrasound using the Chattanooga Intelect Mobile 2 COMBO (DJO France device, ENOVIS) or with acoustic shock waves, administered with the Piezowave, PW2 (Richard Wolf device, ELvation Medical).

For the ultrasound treatment, the well containing the sample was positioned in the central part of the Chattanooga transducer by interposing a thin layer of gel (Stoßwellen gel, ELvation Medical) to ensure acoustic impedance matching. A 2 cm^2 transducer was employed to match the area of a 24-wells plate. Three different US settings, maintaining a frequency of 1 MHz, were evaluated: i) 1 W/cm^2 for 2 min (US1) ii) 2 W/cm^2 for 1 min (US2) iii) 2 W/cm^2 for 2 min (US3).

For the shockwave (SW) treatment, the 6-well plates were stimulated from the bottom by employing a linear focused therapy source, model FBL10 × 5G2 (Richard Wolf device, ELvation Medical), having the possibility to treat the bioprinted tubes for their entire length. To achieve this, a tube holder fabricated in PDMS was used, in order to maintain the tube straight and still while irradiating them with SW. The source was equipped with a gel pad to obtain a penetration depth of 5 mm and a thin layer of gel (Stoßwellen gel, ELvation Medical) was applied between the pad and the 6-well plate. Each administration consisted of 250 shots of high-energy focalized shockwaves with 4 shots/s frequency, at E6 energy level, corresponding to an energy flux density of 0.041mJ/mm^2, following a previously developed protocol [23,28]. For each procedure, a treatment was administered every 24 h for 3 days, similar to what done for ultrasound and schematized in Fig. 2. Control samples were placed in a separate 24-wells plate or 6-wells plate for the US and SW treatments, respectively, and remained completely untreated or were treated with L-ZnO or L-YSA-ZnO only.

2.14. Cell viability assay

A live-dead assay coupled with cell membrane integrity assay was carried out after the combined treatment on 3D CRC models incubated with L-ZnO or YSA-L-ZnO. After 24 h and 96 h from last acoustic treatment, in each well plate 1.5 μM propidium iodine (PI) was added as indicator of membrane integrity. PI is membrane impermeable and able to bind with DNA, thus it can mark cells with damaged membrane. Furthermore 3 mM Calcein-AM as indicator of live cells was added. Namely, Calcein-AM is normally a non-fluorescent component but when the AM group is enzymatically cleaved by intracellular activity of living cells, it emits a fluorescent signal. In order to stain cells within the

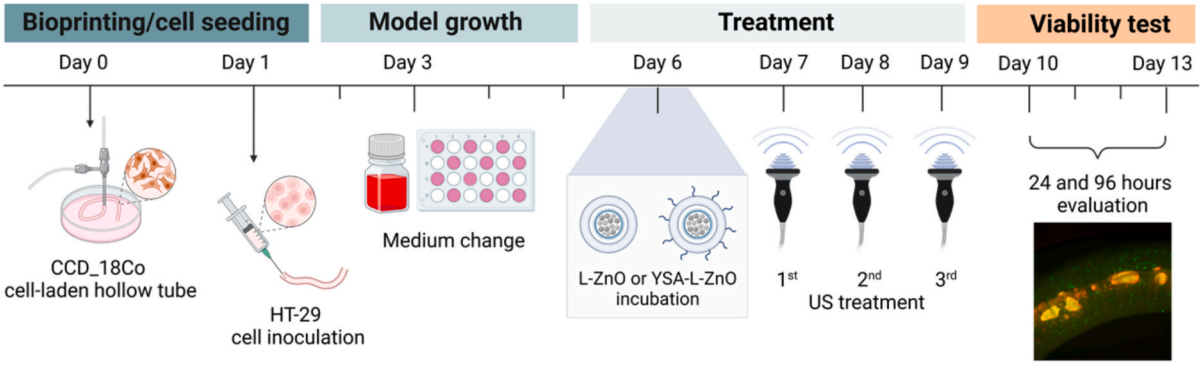

Fig. 2. Scheme of timeline and experimental setting of the colon co-culture tubular conduit model for CRC studies with NPs and stimuli-responsive treatments. CCD-18Co cells were coextruded with Gel11Al2.5 bioink to form cell-laden hollow tube. After 24 h, HT-29 cells were seeded inside the conduits, and the model was cultured for 5 days. On day six, L-ZnO or YSA-L-ZnO were administered to the models, followed by ultrasound treatment on days seven, eight, and nine. Finally, their viability was evaluated 24 and 96 h after the last treatment.

model, fresh culture media containing the abovementioned dyes was added, followed by a 30-minute incubation at room temperature. Cells were then observed under a wide-field fluorescence-inverted microscope (Eclipse Ti-E, Nikon), employing a 4X PlanAPO objective.

2.15. Nanoparticle internalization

To detect the presence of the NPs in the 3D models through fluorescence microscopy, the NPs were labelled. Prior to the lipidic coating, ZnO NCs were labelled with ATTO-647-NHS ester (Sigma). 2 μL of a 2 mg/mL solution were added for each mg of ZnO NCs to a suspension of ZnO NCs in ethanol at 1 mg/mL concentration and stirred overnight at 250 rpm at room temperature. Then, the ZnO NCs were washed by multiple centrifugations (10 min at 14000 x g) followed by resuspension steps in ethanol. After the last centrifugation, the pellet was coated by the lipidic formulations (with either YSA peptide or not, as described above) and resuspended in order to obtain a ZnO NCs concentration of 1 mg/mL. The final suspension was sonicated for 10 min. After 24 h and 96 h from the last acoustic treatment, in each well plate Hoechst dye (6 μg/mL) for nuclei staining was added and, after 30-minute incubation at room temperature, the 3D models were observed under a fluorescence microscope.

2.16. Image processing and color intensity analysis

The inner and outer diameter of the tubes were calculated by acquiring different images of different tube batches after bioprinting. In each image the inner and outer diameter was calculated in five different points. All measurements are reported in micrometers (μm), and the error bars were calculated based on a 90 % confidence interval.

Subsequent image processing and analysis were performed using Image J software. Quantitative analysis of PI/calcein-AM fluorescence in the 3D CRC-stained model were conducted by pre-dividing each image into three distinct regions of interest (ROI): the background, the walls of the conduit containing CCD-18 cells and the HT-29 organoids in the lumen. For each ROI, the mean grayscale intensity was measured. The relative intensity of the cell regions (walls and organoids) was calculated by comparing the mean intensity of these regions to that of the background and was expressed as a percentage. To determine the cell survival rate, all values were normalized to the initial cell survival rate at the time of printing or seeding. All measurements were conducted at least in triplicate, the average values were used for statistical analysis and presented as a heat map.

2.17. Figures

All the graphs were created in GraphPad Prism 9 and all the schemes were produced with BioRender.com.

2.18. Statistical analysis

All the presented biological tests were carried out at least in triplicate and One-way ANOVA and T tests were performed with GraphPad Prism 9; *$p < 0.05$, **$p < 0.005$, ***$p < 0.0005$.

3. Results and discussion

3.1. Bioink optimization

The development of a functional 3D CRC model required careful consideration of both the bioink formulation and the implementation of an advanced bioprinting technique to recreate the complex architecture of colorectal tumors. This study focused on optimizing a cytocompatible bioink composed of two natural polymers capable of mimicking the extracellular matrix and enhancing the biological performance of cells. In the fields of tissue engineering, alginate is utilized to provide a biocompatible structural scaffold for cell growth, exploiting its extensive properties, which include long-term stability conferred by its chelating ability [29]. Moreover, its shear-thinning behavior, elastic properties, and rapid crosslinking capability make it one of the most commonly used biopolymers for hydrogel formation in 3D bioprinting [30]. Despite its favorable properties, alginate lacks the ability to be recognized by cells and support cellular proliferation [31]. For this reason, in this research, to increase cytocompatibility and help the proliferation of encapsulated cells, alginate was blended with gelatin developing a composite bioink. Indeed, gelatin, a biocompatible and thermosensitive material derived from collagen, the most abundant protein in the human body, was chosen for its highly biomimetic characteristics and the ability to promote cell adhesion, as it contains the arginine-glycine-aspartic acid (RGD) motif. In addition, gelatin over its gelation point alters the viscosity of the bioink, enabling a more consistent and homogeneous extrusion. The combination of these natural polymers resulted in the creation of a hydrogel with excellent mechanical properties, capable to be processed under mild conditions and suitable for application in 3D coaxial bioprinting [32]. Different concentrations and combinations of gelatin and alginate have shown to possess a considerable influence on rheological properties, shear stress tolerance, gelation process efficiency and long-term stability of the composite 3D CRC model [33]. To this end, six distinct formulations of the composite bioink were prepared using three different solvents (as summarized in Table 1). These formulations were successfully printed and tested (see the most representative results depicted in Fig. 3), resulting in the selection of the optimal solution.

Actually, modifying the polymers concentrations had a marked

Table 1
Combinations of alginate and gelatin solution to obtain an optimal printable bioink: solvent combinations, polymers weights, abbreviations for the various bioink formulations, and the corresponding optical microscopy image in Fig. 3 of the hollow tube after the 3D coaxial bioprinting.

	Gelatin	Alginate	*Figure*
bdH_2O			
Gel8Al1	8 %	1 %	***3.A***
Gel10Al1	10 %	1 %	***3.B***
Gel15Al1	15 %	1 %	***3.C***
Physiological solution			
Gel15Al1	15 %	1 %	***3.D***
Cell culture medium			
Gel15Al1	15 %	1 %	***3.E***
Gel8Al2	8 %	2 %	***3.F***
Gel11Al3	11 %	3 %	***3.G***
Gel11Al2.5	11 %	2.5 %	***3.H***

impact on the viscoelastic properties and printability of the bioink, as well as on the final shape and stability of the 3D tubular model.

Initial experiments used bdH_2O and physiological solution as solvents. Studies have reported that the ionically crosslinked alginate loses the crosslinking calcium ion stability in the presence of calcium chelators (e.g., phosphates), monovalent ions (e.g., K+, Na+, etc.), and non-crosslinking divalent ions (e.g., Mg2 +). However, alginate gels remained stable in cell culture media due to some calcium ions in the media to counteract the losing effects [33,34].

3.2. Bioink characterization

All bioinks (summarized in Table 1) exhibit non-Newtonian shear thinning behavior (Fig. 3J). Viscosity is obviously affected by the percentage of polymers present, but additionally it appears to be more closely related to the alginate content. This is consistent with previously reported results [35–37]. In fact, given the same gelatin content, a higher percentage of alginate results in a more viscous bioink. In general, viscosities are in the range of 10^1-10^2 Pa•s at low shear rates (0.001 s^{-1}) and of 10^0 Pa•s at high shear rates (1000 s^{-1}); those values are comparable with reported values for injectable gels [38–40]. These properties have a significant impact on the bioink printing process. Specifically, increasing the alginate concentration (Ge11Al3) significantly altered the viscosity of the bioink, resulting in an increase of shear stress values and changes in the physical properties of the hollow tubes, which then exhibit wrinkles and increased rigidity (Fig. 3G). Conversely, decreasing the alginate concentration (Gel15Al1, Gel10Al1, Gel8Al1) improved the flow dynamics of the bioink, but led to structures with short-term stability, which tend to collapse rapidly (Fig. 3A-E). Increasing gelatin percentage facilitated the printability of the bioink, but resulted in conduits that could not maintain their shape for extended periods (see Fig. 3C-E). The combination of increasing alginate and reducing gelatin (Gel8Al2) produced hollow tubes that lacked elasticity and presented a more challenging extrusion process, due to the increased density and viscosity of the bioink (Fig. 3F). Finally, the optimum printability and durability of the tubular models were obtained at 11 % gelatin and 2.5 % alginate in cell medium (Gel11AL2.5), resulting in the generation of organized and stable hollow tubes able to maintain their shape and properties for more than 13 days. Based on the previous results, this formulation was selected for subsequent experiments as it allowed to obtain a bioink suitable for bioprinting and to realize 3D models with well-defined structures and features as shown in Fig. 3H. To further demonstrate the structural stability and uniformity of this model, measurements of both inner and outer tube diameters were taken. After bioprinting, images of the conduits of different batches were acquired, and five measurements of both inner and outer diameters were taken from each image and averaged (Table S1). The average dimensions of the inner and outer diameters were respectively 922.32 ± 19.17 μm and 1696.08 ± 24.71 μm, while the standard deviation 125.00 μm and 161.12 μm, as reported in Fig. 3I.

Concerning the temperature behavior, this ink showed, as expected, a decrease of viscosity around 37 °C, related to denaturation of gelatin (Fig. 3K). This transition temperature was selected by performing frequency sweep test (Fig. 3L), which showed a biphasic system transitioning to the gel phase: below the crossover frequency (around 80 rad/s) the bioink behaves like a sol (G'' > G'), while at higher frequencies it exhibits a gel-like behavior (G' > G''). The fact that the loss modulus prevails over the storage modulus at low frequencies can be attributed to the presence of alginate, which has a more viscous-like behavior. This behavior becomes less evident at high frequencies where, in fact, G' appears to be higher than G'' [41].

3.3. Two-step crosslinking method

Having established the conditions to successfully prints tubes, The bioprinting of was achieved through a two-step crosslinking method. As detailed in the materials and methods section, alginate undergoes gelation upon contact with bivalent Ca^{2+} ions, which interact with the glucuronic acid blocks in the alginate chains [17]. At the same time, during the extrusion, the gelatin undergoes instantaneous thermal gelation due to a decrease in temperature (see rheology results). Gelatin actually transitions from a random coil conformation at 40–50 °C to a triple helix conformation, similar to collagen, when cooled down below 35 °C. To stabilize this conformational change at incubation temperature, the gelatin was further covalently crosslinked by mTG, a U.S. Food and Drug Administration-approved enzyme, which catalyzes the formation of amide bonds between lysine and glutamine residues in the gelatin [42].

The use of a coaxial needle allows for the simultaneous extrusion of bioink and $CaCl_2$ from the outer layer and core of the coaxial nozzle, respectively. Adjusting the concentrations of alginate and the crosslinker enabled precise control over the gelation kinetics. The combination of alginate's phase transition in the presence of bivalent cations and the gelation of gelatin facilitated the creation of 3D hollow perfusable tubular conduits, as depicted in Fig. 4.

3.4. Characterization of the cross-linked tube

Bioinks crosslinked with $CaCl_2$ alone and with $CaCl_2$ and mTG were characterized in terms of amplitude sweep. The bioink crosslinked with $CaCl_2$ (Fig. 5A) exhibits predominantly solid-like behavior in the analyzed region. The linear behavior over 3 decades of strain is consistent with the presence of physical crosslinking (ionic bonds), which are not directional and lead to a progressive disentanglement of the polymeric chains as the strain increases, with a consequent decrease of G'. Differently, after transglutaminase crosslinking, two characteristics can be observed (Fig. 5A): firstly, an increase of G', which is consistent with the formation of an additional chemical network, which leads to an increase of crosslinking density and rigidity; secondly, it can be observed a drop of G' above 500 % of strain, which can be related to breakage of crosslinking points, and consequently loss of material consistency. This behavior was evidenced by an amplitude burst test in time (Fig. 5B). In this case, the sample was first tested at fixed strain (50 %) at a frequency of 1 Hz. Then, the material was deformed for 10 s at a strain of 1000 % and afterwards sampled at 50 % strain again. As expected, the gel physically crosslinked does not undergo breakage and mechanical properties are almost constant even after high deformation. Differently, the sample crosslinked with $CaCl_2$ and mTG experience breaking of the chemical bonds and a drop of mechanical properties (more than one order of magnitude decrease). From this test emerges that a gel with better properties in terms of stability can be obtained through transglutaminase crosslinking; on the other hand, this cannot be deformed indefinitely, but with a maximum strain deformation of around 500 %, which in any case is suitable for the intended application.

Mechanical tests were conducted to evaluate key mechanical

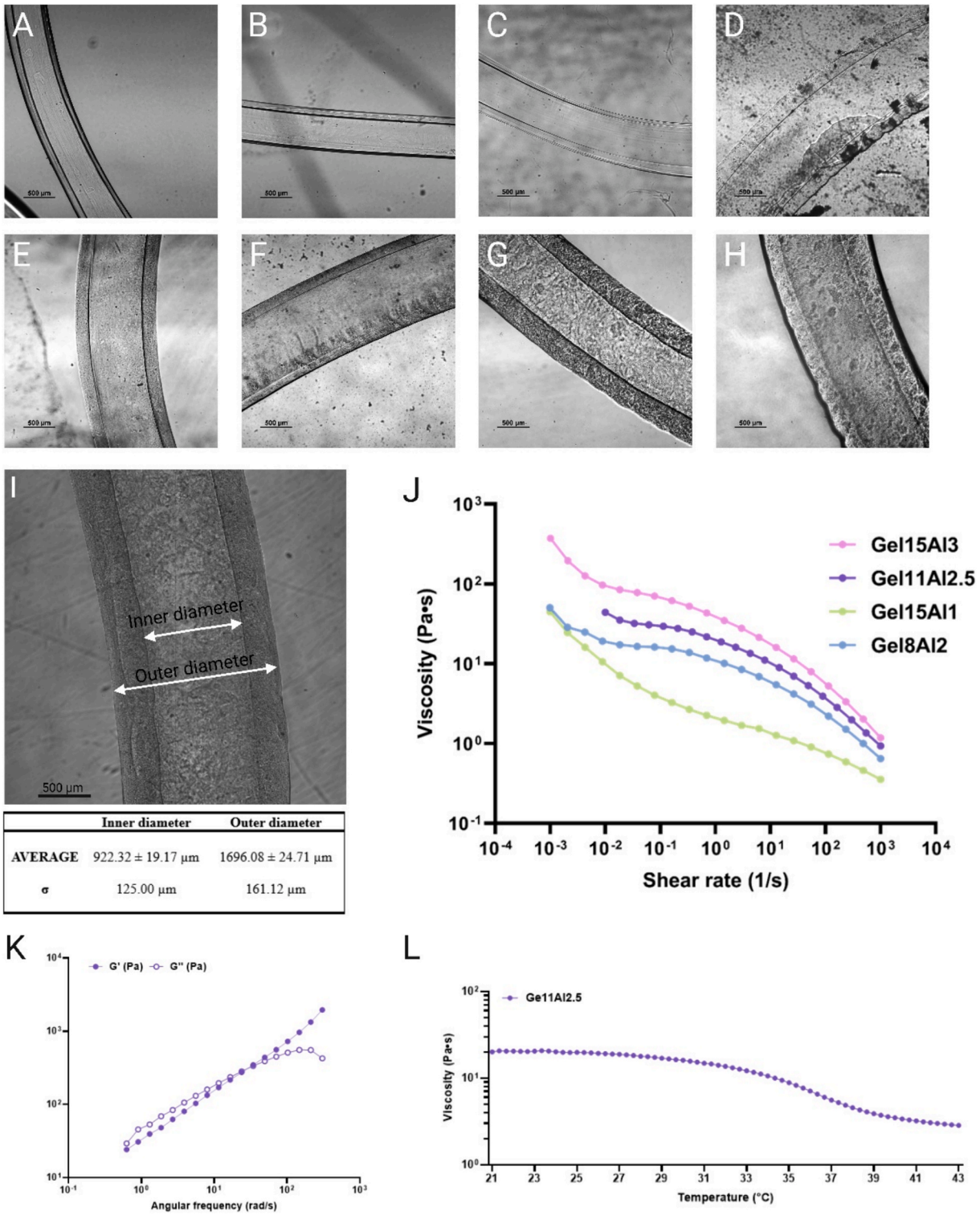

	Inner diameter	Outer diameter
AVERAGE	922.32 ± 19.17 µm	1696.08 ± 24.71 µm
σ	125.00 µm	161.12 µm

Fig. 3. Results of distinct formulations of the composite bioink prepared using different solvents after coaxial extrusion: **(A)** Gel8Al1 in bdH_2O; **(B)** Gel10Al1 bdH_2O; **(C)** Gel15Al1 bdH_2O; **(D)** Gel15Al1 in physiological solution (0.9 %wt NaCl); **(E)** Gel15Al1 in cell culture medium; **(F)** Gel8Al2 in cell culture medium; **(G)** Gel11Al3 in cell culture medium; **(H)** Gel11Al2.5 in cell culture medium; **(I)** Scheme of diameter measurements and corresponding average ± errors values and standard deviation for inner and outer conduit diameters. **(J)** Viscosity of different concentrations of the bioink at different shear rate; **(K)** Viscosity of Gel11Al2.5 bioink at different temperatures; **(L)** G' and G'' of Gel11Al2.5 bioink changing the angular frequency.

features of the optimal bioink, such as Young's modulus and elongation at break, which are crucial information in view of bioapplication. Tensile test was performed on 8 specimens at a rate of 10 mm/min bringing them to failure. Fig. 5C shows a representative stress–strain curve. The Young's modulus value measured was of 17.13 kPa (± 3.06). This value is in line with the values averagely found for colorectal cancer tissue (7.51 kPa) [43], which are in turn reported to be significantly higher than that of normal colorectal tissue. However, higher values can be also found in the literature, i.e. about 300 kPa for elastic modulus of biological colorectal tissue [44]. It is worth mentioning that the Young's

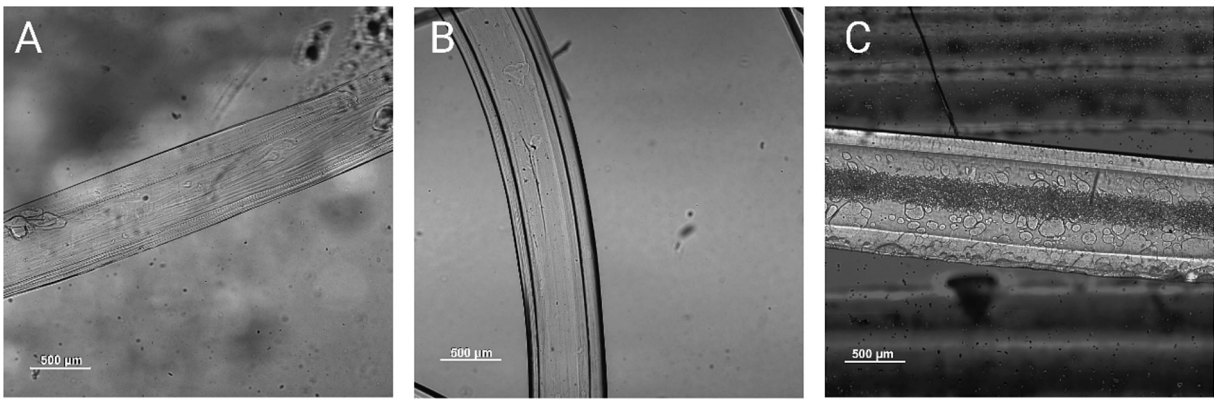

Fig. 4. Optimal 3D tubular construction at day 7 after crosslinking. **(A)** 3D tubular construct obtained by ionic crosslinking of alginate chains; **(B)** Two-step crosslinking obtained through ionic crosslinking of alginate chain and covalent crosslinking of gelatin; **(C)** Further crosslinking of the conduits with a $CaCl_2$ ambient spray resulting in roughened walls.

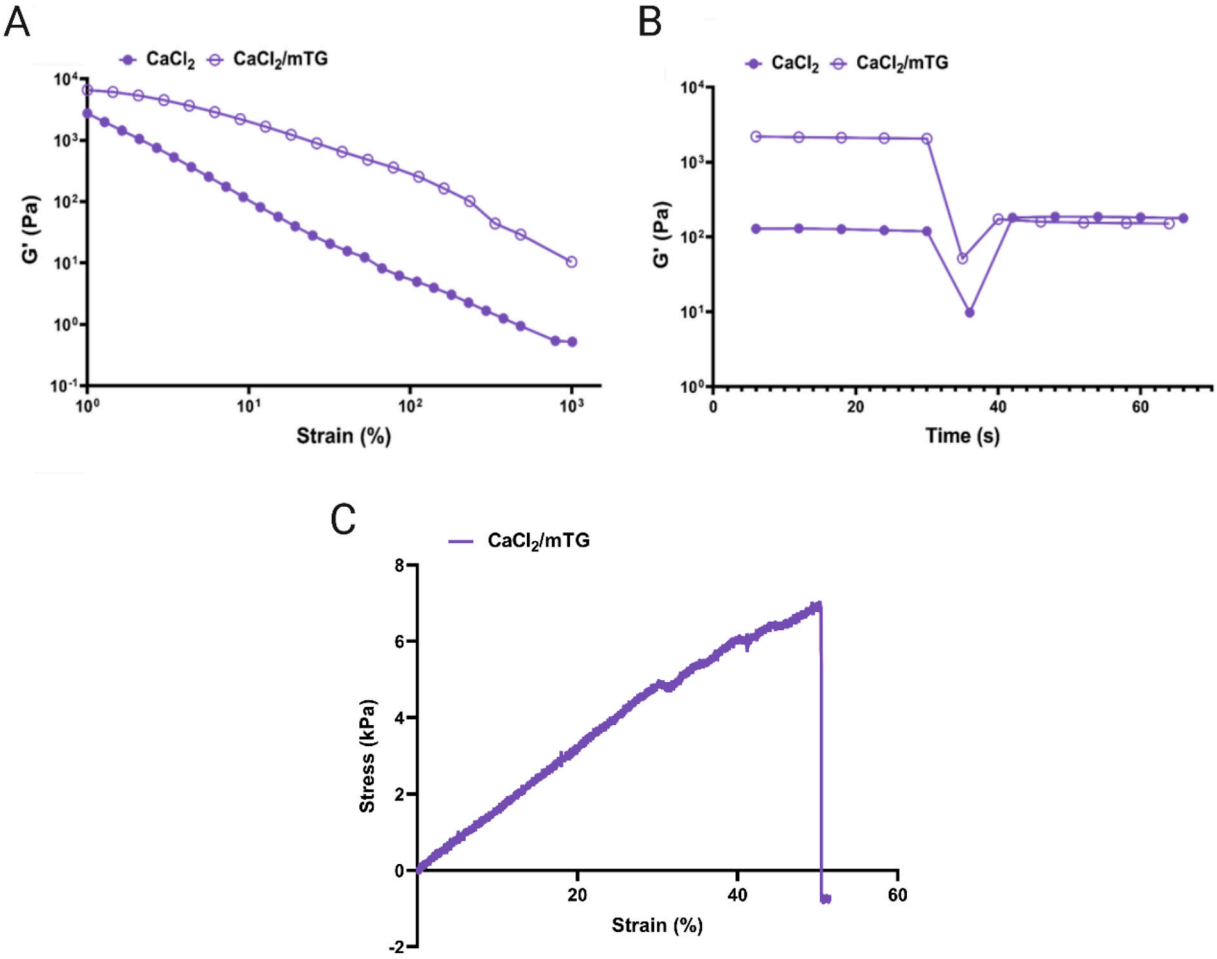

Fig. 5. **(A)** Amplitude Sweep of the optimal bioink crosslinked with $CaCl_2$, compared to the bioink crosslinked with both $CaCl_2$ and microbial transglutaminase; **(B)** Amplitude Burst in time strain from 50 % to 1000 % bioink crosslinked with $CaCl_2$, compared to the bioink crosslinked with both $CaCl_2$ and microbial transglutaminase **(C)** Stress–strain curve of a dumbbell-shaped specimen under tensile testing. The curve is representative of the mechanical response observed across all samples tested at a rate of 10 mm/min.

modulus value of our 3D cross-linked tube is obtained from the material without cells, Possibly, the Young modulus value of cell-laden material would be higher [45], considering a possible increase in stiffness after cell colonization, but still in line with the broad values found in the literature. The elongation at break value 48.5 % (± 6.9) is also comparable to that of biological tissue [46], confirming the potential of this bioink in making a colorectal model. Further data are reported in Fig. S1.

3.5. Cells encapsulation and seeding

A more comprehensive model was developed by incorporating

colorectal cells, which replicates essential features of the disease, including proliferation, invasion, and therapeutic response. To closely mimic the native cellular environment, cells from the normal human colon tissue CCD-18Co cell line were blended in the bioink, enabling the bioprinting of biologically relevant colorectal constructs. Although cell lines do not fully capture patient-specific heterogeneity, we selected a CRC line classified as a microsatellite stable (MSS) [47]. In the literature, HT-29 cell line is widely used in drug testing and therapy response studies due to its molecular relevance to CRC, stability, and suitability for 3D printing and tumor-stroma applications. Its molecular profile aligns with a significant subset of real CRC cases, making it a relevant model for evaluating therapeutic responses [48]. The HT-29 human colorectal adenocarcinoma cell line was instead seeded inside the tubular bio-constructs to more accurately simulate the natural tumor environment, forming tubular conduits that reflect the architecture and biological dynamic of CRC. Factors influencing cell viability during the bioprinting process, such as shear and thermal stresses, extrusion technique and parameters, as well as gelation conditions, were carefully evaluated. Interestingly, our results indicated that changes in cell density had a minimal effect on viability (data not presented). In contrast, the variation in bioink viscosity was found to significantly impact the cell viability. This suggests that the rheological properties of the biomaterial and the extrusion process using a nozzle-based technique are the crucial parameters to be controlled to maintain the cell viability [19].

In this study, the previously characterized bioink composition, Gel11Al2.5, was mixed with a CCD-18Co concentration of 2 x 10^6 cells/mL before the extrusion. Cell viability, migration, and interactions were evaluated through viability assays on days 1, 8 and 13 after extrusion. The results, quantified by Calcein-AM staining, showed no significant changes in cell viability over the observation period, indicating sustained viability after two weeks and the high cytocompatibility of the selected bioink. Cells appeared as isolated entities within the hydrogel matrix, with their distribution remaining unchanged over time. Fluorescence microscopy confirmed that the cells were homogeneously distributed throughout the bioprinted constructs, which retained their structural integrity over 13 days (Fig. 6A). Similar evaluations were conducted for acellular hollow tubes seeded within the internal lumen with a concentration of 1 x 10^7 cells/mL HT-29 cell line. In this case, cell viability remained high throughout the study period, although the cell configuration evolved over time. As illustrated in Fig. 6B, single cells gradually formed compacted masses over time. Following the assessment of cytocompatibility and stability of the bioink and the extrusion process, the final 3D CRC model was obtained integrating the two previously developed models (Fig. 6C). Under the same conditions and parameters, a co-culture of healthy and CRC adenocarcinoma cell lines was established and grown for 13 days. During this period, the model closely mimicked the *in vivo* tumor microenvironment, allowing for the study of cell interactions with targeted or untargeted NPs and the responses to innovative acoustic waves treatments. To assess cell viability, the intensity of pixels derived from Calcein-AM staining, which indicates viable cells, was quantitatively evaluated through an Image J routine. The resulting data, presented in Fig. 6D, are related to the viability of both normal CCD-18Co cells in the tube walls, the HT-29 tumor aggregates in the lumen and the co-culture models. The analysis was normalized to viability on the first day of printing or seeding. A slight decrease in cell viability was observed initially across all groups, followed by a stabilization phase. This decline in viability could reflect an initial period of cellular adjustment, with cells possibly undergoing stress as they adapt to the new conditions. However, over time, viability stabilized, suggesting that the cells eventually continued to proliferate and evolve in the conduits. Additionally, the variability in the results can

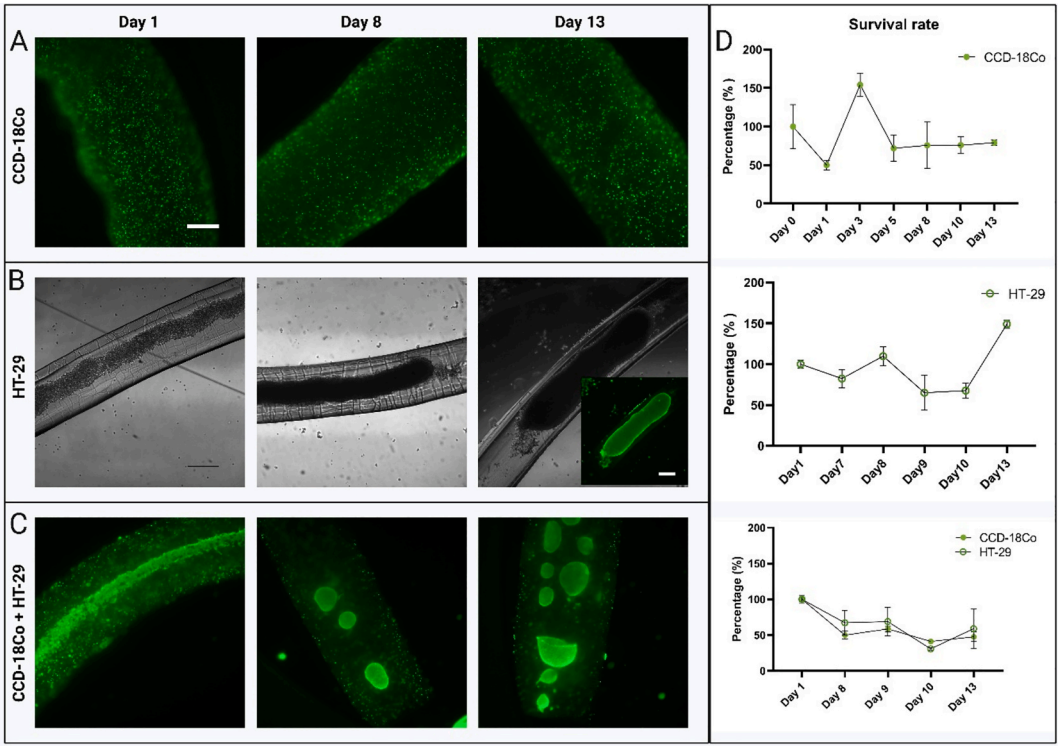

Fig. 6. Cell viability evaluation and cellular assembly over 13 days. **(A)** Fluorescence images of 2 x 10^6 cells/mL CCD-18Co cell line encapsulated in bioprinted conduits at day 1, 8 and 13 after extrusion; **(B)** Fluorescence images of 1 x 10^7 cells/mL HT-29 cell line seeded inside acellular bioprinted hollow conduits at day 1, 8 and 13 after extrusion; **(C)** Fluorescence images co-culture of HT-29 and CCD-18Co at day 1, 8 and 13 after extrusion. CCD-18Co and HT-29 were stained with Calcein-AM (green). Scale bar: 500 μm, **(D)** Quantitative evaluation of the intensity of the Calcein-AM (green) signal at different time points using Image J. Cell viability percentage was assessed by measuring the mean intensity of the fluorescent signal in each image, differentiating between CCD-18Co and HT-29 cells signal. (For interpretation of the references to color in this figure legend, the reader is referred to the web version of this article.)

be attributed to differences in cell concentration and organization across different batches of conduits. Nonetheless, the high viability observed in these experiments highlights the potential of bioprinting cells within the construct and their capability to adjust and proliferate in this 3D co-culture system.

4. Proof of concept

4.1. NPs specific tumor targeting

To reduce the dose-dependent toxicity of ZnO NCs and stabilize the nanocrystals in biological environments, they were coated with a phospholipidic coating (L-ZnO), while conjugation with the peptide YSA (YSA-L-ZnO), specifically targeting the Ephrin A2 (EphA2) receptor [27], was employed to enhance internalization in CRC cells, compared to non-targeted counterparts. The high expression of the EphA2 receptor in CRC cell lines is well-documented in the literature and was confirmed by analyses conducted in a previous study [23], which also demonstrated that the HT-29 cancer cell line exhibited a higher tendency to uptake YSA-L-ZnO compared to CCD-18Co, in both 2D cell culture and 3D spheroidal configurations [23]. The effectiveness of the coating was evaluated through dynamic light scattering (DLS) and zeta potential, while the YSA-L-ZnO were investigated through fluorescence microscopy, (reported respectively Fig. S2 and Fig. S3). To effectively evaluate the distribution of solid-state nanoparticles in a 3D model and their capacity to target the specific tumor mass with respect to the healthy cells, a 3D qualitative internalization test on the co-culture model was performed. Here in particular the role of biomimetic NPs equipped with the YSA targeting peptide was assessed in the distribution in the 3D model.

The bioprinted models were incubated with fluorescent labelled nanoparticles and analyzed through spinning disk microscopy 24 h post

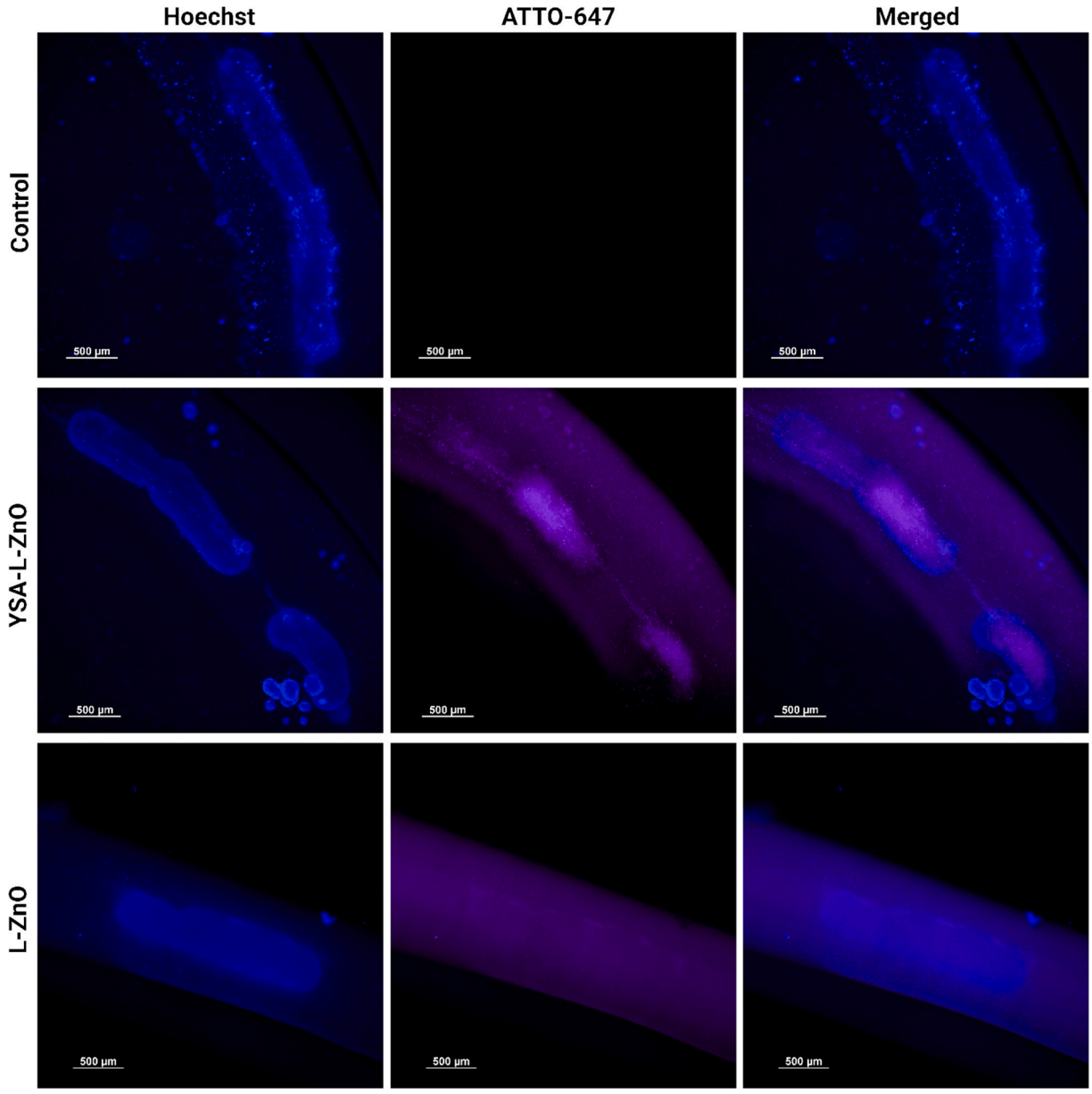

Fig. 7. NPs uptake in 3D CRC models. 3D CRC models were extruded, seeded and grown for 5 days and left untreated (control), treated with targeted nanoparticles (YSA-L-ZnO at 200 µg/mL) or not targeted ones (L-ZnO at 200 µg/mL). After 24 h from the administration of the nanoparticles (day 6), the 3D models were stained with Hoechst dye (blue) to mark cell nuclei, while nanoparticles were previously labelled with Atto-647 (purple). (For interpretation of the references to color in this figure legend, the reader is referred to the web version of this article.)

administration. Qualitative images show the tendency of the YSA-L-ZnO, compared to L-ZnO, to be consistently taken up by CRC cells. Fig. 7 shows the untreated control cells (upper row), YSA-L-ZnO (middle row) and L-ZnO (lower row) where the nuclei are visible in blue and the ZnO core in purple.

4.2. Stimuli-responsive nanoparticles treatment in CRC bioprinted models

As proof of concept, to better replicate potential *in vivo* conditions involving 3D structures, a stimuli-responsive treatment combining nanoparticles administration and acoustic pressure waves irradiation was applied to the previously characterized 3D CRC models. Fig. 2 presents a schematic representation of the combined treatment which encompasses the extrusion and growth of the model, the application of treatments, and the final evaluation of cell viability. In earlier studies by our group, the combination of iron-doped zinc oxide nanocrystals and acoustic pressure stimulation (either via ultrasound or shock waves) was shown to trigger cytotoxic response in biological systems [23,49]. Extensive research has been conducted on the generation of reactive oxygen species (ROS) following exposure of ZnO micro- and nano-materials to ultrasound irradiation [50,51]. This effect can be harnessed in cancer therapy, as elevated levels of intracellular ROS, along with sonochemical damage and sonothermal effects, are highly effective in killing cancer cells [52,53]. Continuous ultrasound and NPs combined treatment.

To assess the effectiveness of this customized CRC model, US stimuli were applied to NPs-treated CCD-18Co and HT-29 cells 3D models. The ultrasound was generated using a Chattanooga Intelect Mobile 2 COMBO device, with three different combinations intensity and duration tested (US1: 1 W/cm^2 for 2 min, US2: 2 W/cm^2 for 1 min, US3: 2 W/cm^2 for 2 min). Initially, the co-cultured model was incubated for 24 h with L-ZnO and their targeted counterpart, YSA-L-ZnO, followed by a triple ultrasound treatment. Cell viability of HT-29 and CCD-18Co was evaluated at 24 and 96 h post-treatment (according to the scheme in Fig. 2) using fluorescence microscopy (Fig. 8A). To produce quantitative results, the intensity of pixels derived from the PI-stained cells (i.e. the dying ones) has been collected and evaluated through an Image J routine, producing the heat color map in Fig. 8B, related to the viability of both normal CCD-18Co cells in the tube walls and the HT-29 tumor aggregates in the lumen. Statistical analyses are reported in Table S2 and S3.

Notably, over the 13-days period, the 3D models retained their structure, providing a stable environment ideal to cell growth and experimentation. This proof of concept demonstrates that both CRC cells in the lumen and healthy colon cells embedded in the bioink remained viable after both 24 and 96 h from the last US treatment.

Also interestingly, the use of NCs, either targeted or not, is proved to be highly safe for the colon model, both for the healthy and the tumoral cell structures. This result further confirms the high biocompatibility of these lipid-coated ZnO NCs, as also proved by us in previous works [23,26] and the suitability of our 3D bioprinted model.

Concerning the combination with US, three different settings were tested: US1 and US3 settings both last for 2 min of irradiation time but apply different ultrasound intensities (1 W/cm^2 and 2 W/cm^2, respectively). In contrast, US2 setting applies the same intensity as US3, but for a shorter irradiation time (1 min).

In the resulting therapeutic treatments, the combination of YSA-L-ZnO with US1 and US3 provoked greater damage compared to the other US2 configuration when considering the 24 h time evaluation. This trend remained evident even at 96 h. However, a more pronounced decrease in viability is also evident in both control groups treated with ultrasound alone (either US1 or US3). In particular, since the US3 treatment alone already causes harmful effect to cells in the 3D in vitro model, we just evaluated the combined effect with the targeted NPs, YSA-L-ZnO. As clear from the images in the last row of Fig. 8A, we did not identify safe conditions with US3 to propose an effectively stimuli-responsive therapy, i.e., being fully biocompatible when the two stimulations (ultrasound and nanoparticles) are applied individually, but highly toxic when applied in combination. This is the reason why the sample L-ZnO and US3 was not evaluated.

Concerning the treatment with US2, an initial decay in cell viability is evident after 24 h in both the control group (US2 alone) and the combination treatment one (NPs + US2). A viability recovery is observed after 96 h, with a more pronounced cytotoxicity in the combined treatment group than the control one.

From these findings, it is believed that US2 is the preferred US application setting, because it allows not to damage the colorectal tissues over long time ranges (96 h) producing the therapeutic action only in combination with the NPs, in particular with the targeted ones.

4.3. Acoustic shockwaves and NPs combined treatment

As a second proof of the concept, acoustic shockwaves were applied to the 3D CRC tube model based on protocols and results established in our previous studies with a single point probe [23,28]. In accordance with the previously described therapeutic set up used for continuous ultrasound, three consecutive SWT were administered at 24, 48 and 72 h post-NP administration, as schematized in Fig. 2. A linear focusing SW applicator was employed to guarantee a homogeneous application over the whole tube length. The fluorescence microscopy results are presented in Fig. 9A for a visual live-dead assay. Likewise, to produce quantitative results, a heat color map was obtained through an Image J routine and is shown in Fig. 9B. Statistical analyses are reported in Table S4 and S5.

The data shows that these tubes are not in general as healthy as in the previous case depicted in Fig. 8. Probably, this inferior cell viability of the control and NPs treated bioprinted tubes can be due to the use of 6-well plates and the PDMS holder to maintain the tube straight, which can reduce the amount of nutrients provided to the living cells in the tubes' wall and internal lumen.

Starting from this consideration, it is evident that the treatment with the sole use of SW does not importantly impact the cell viability of the healthy CCD-18Co line, while it affects more importantly the viability of cancer HT-29 cells. The presence of targeted YSA-L-ZnO NPs affects the cell viability, specifically of the tumor components after 24 and especially at 96 h. The combined treatment between targeted NPs and SW after 24 h and 96 h results in an important reduction of cancer cell viability, while the healthy counterpart remains almost unaffected with respect to the control cases (untreated, NP-only and SW-only). The use of untargeted L-ZnO NPs has a moderate effect on cell viability on both healthy and cancer cells and no specific augmentation of efficacy is observed when applying the SW.

As a whole, these data prove that also the use of acoustic shockwaves can be performed on 3D colorectal cancer models and that the presence of site-selective and targeted NPs can allow to specifically exploit a therapeutic action against cancer cells while sparing healthy cell counterpart. However, future refinements on the 3D bioprinted tube positioning should be made for adopting in vitro this specific SW set-up.

5. Conclusions

In this work we have reported the development of a bioink to print a 3D coaxial extrusion of tubes laden with a co-culture of cells. We have adopted the model to reproduce the tri-dimensional structure of colon and uploaded healthy cells in the tube's walls while culturing spheroidal structures of colorectal cancer cells in the inner lumen. In this way we have tried to approach the pathophysiological geometry of an established colorectal adenocarcinoma. With this 3D model, after proper characterization of the bioink and of the finalized tubes, we have then tested the cell viability and the possible targeting efficacy in 3D of a selected type of NPs, here core–shell lipid-coated zinc oxide nanocrystals, decorated with a peptide specific for the Ephrin A2 receptor

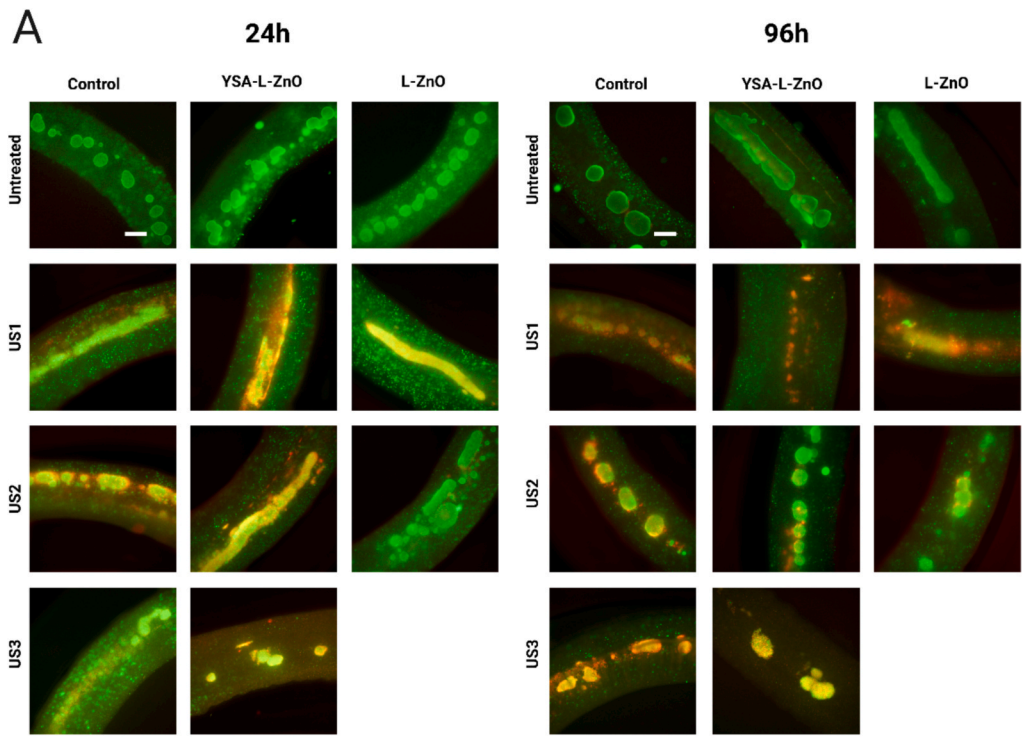

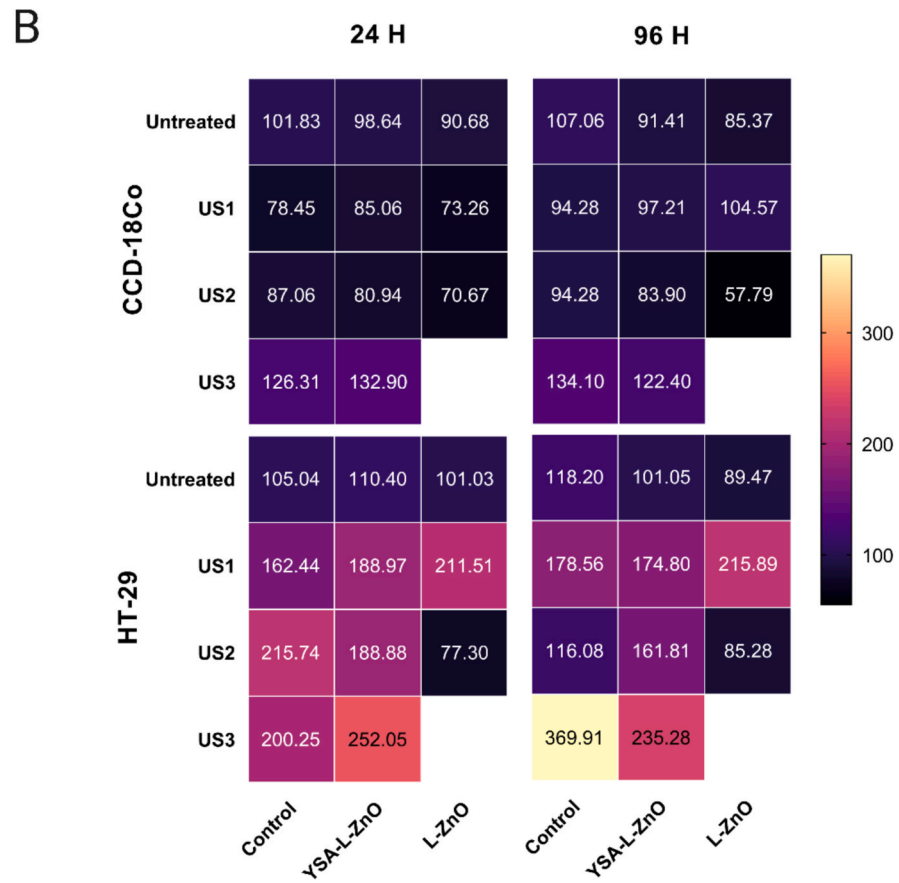

(caption on next page)

Fig. 8. A) Effect of the ultrasound and YSA-L-ZnO or L-ZnO NPs combined treatment in CRC co-culture models. The 3D models were cultured for 6 days and left untreated or treated with nanoparticles (YSA-L-ZnO or L-ZnO at 200 μg/mL). After 24, 48 and 72 h, the models were subjected to a US treatment at three different US settings (US1: 1 W/cm^2 for 2 min, US2: 2 W/cm^2 for 1 min, US3: 2 W/cm^2 for 2 min). Control was left untreated. After 24 and 96 h from the last treatment, cell viability was evaluated through florescence imaging. Cells were stained with Calcein-AM (green) and PI (red) to mark live and dead cells, respectively. Scale bar: 500 μm; **B)** Heat Map to quantitatively evaluate the intensity of the PI (red) signal after the ultrasound and YSA-L-ZnO or L-ZnO NPs combined treatment in CRC co-culture models using Image J. Cell mortality percentage was assessed in the previous experiments by measuring the mean intensity of the PI signal in each image, differentiating between CCD-18Co and HT-29 cells signal. Control experiments are also reported for comparison. Higher viability is reflected by darker colors (black to blue and to dark violet). Lower viability by pink to yellow colors. (For interpretation of the references to color in this figure legend, the reader is referred to the web version of this article.)

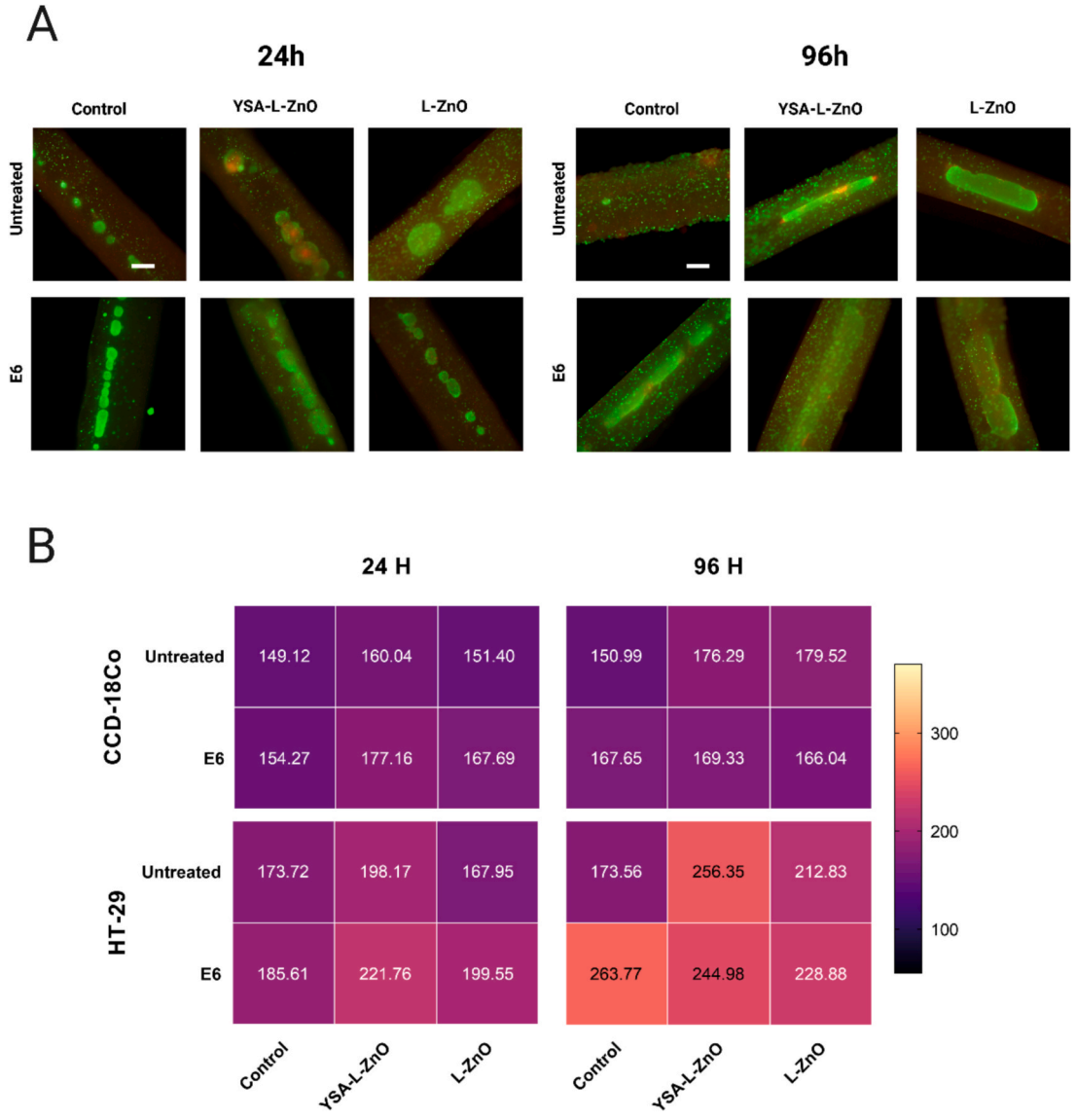

Fig. 9. A) Effect of the shockwave and YSA-L-ZnO or L-ZnO NPs combined treatment in CRC co-culture models. The 3D models were cultured for 6 days and left untreated or treated with nanoparticles (YSA-L-ZnO or L-ZnO at 200 μg/mL). After 24, 48 and 72 h, the models were subjected to a SWT, consisting of 250 shots of high-energy focalized shockwaves at 4 shots/s at E6 energy level (0.041mJ/mm^2). Control was left untreated. After 24 and 96 h from the last treatment, cell viability was evaluated through florescence imaging. Cells were stained with Calcein-AM (green) and PI (red) to mark live and dead cells, respectively. Scale bar: 500 μm; **B)** Heat Map to quantitatively evaluate the intensity of the PI (red) signal after the shockwave and YSA-L-ZnO or L-ZnO NPs combined treatment in CRC co-culture models using Image J. Cell mortality percentage was assessed in the previous experiments by measuring the mean intensity of the PI signal in each image, differentiating between CCD-18Co and HT-29 cells signal. Control experiments are also reported for comparison. Higher viability is reflected by darker colors (black to blue and to dark violet). Lower viability by pink to orange and to yellow colors. (For interpretation of the references to color in this figure legend, the reader is referred to the web version of this article.)

overexpressed in the used CRC cell model, HT-29. After assessing the effective NPs biodistribution, we have proposed an unconventional stimuli-responsive therapy enabled by the specific targeting of such NPs and their activation by acoustic pressure waves, testing both continuous ultrasound and shockwaves. In both scenarios we have observed, with some variations, the efficacy of the treatment, especially over long time periods (96 h) against the cancer cell structures and the good biocompatibility of both NPs and acoustic waves on healthy cell structures in

the tube walls.

As a whole, the developed 3D bioprinted tube represents a promising model for CRC to be used as in vitro biological twin to evaluate novel therapeutic treatment modalities and allowing to reduce the use of living animal models for the first screenings and tests.

Funding sources

This work has received funding under Next Generation EU and the National Plan for Complementary Investments to the NRRP, project "D34H—Digital Driven Diagnostics, prognostics and therapeutics for sustainable Health care" (project code: PNC0000001), Spoke 4 funded by the Italian Ministry of University and Research.

CRediT authorship contribution statement

Giorgia Savino: Writing – original draft, Visualization, Validation, Investigation, Data curation. **Giada Rosso:** Writing – review & editing, Validation, Methodology, Investigation, Data curation. **Maria D'Aloia:** Writing – review & editing, Validation, Investigation. **Ignazio Roppolo:** Writing – review & editing, Supervision, Methodology, Investigation, Data curation. **Valentina Cauda:** Writing – review & editing, Writing – original draft, Supervision, Resources, Project administration, Funding acquisition, Conceptualization.

Declaration of competing interest

The authors declare the following financial interests/personal relationships which may be considered as potential competing interests: Valentina Cauda reports financial support was provided by National Plan for Complementary Investments to the NRRP. If there are other authors, they declare that they have no known competing financial interests or personal relationships that could have appeared to influence the work reported in this paper.

Acknowledgment

This work has received funding under the National Plan for Complementary Investments to the NRRP, project "D34H—Digital Driven Diagnostics, prognostics and therapeutics for sustainable Health care" (project code: PNC0000001), Spoke 4 funded by the Italian Ministry of University and Research. The authors wish to thank the company ELvation Medical GmbH for providing the instrument PiezoWave PW2 from Richard Wolf. The fruitful discussion and preliminary work of Alessandro Bentivogli and Dr. Giulia Mesiano is also gratefully acknowledged.

Appendix A. Supplementary data

Supplementary data to this article can be found online at https://doi.org/10.1016/j.matdes.2025.114478.

Data availability

Data will be made available on request.

References

[1] F. Bray, J. Ferlay, I. Soerjomataram, R.L. Siegel, L.A. Torre, A. Jemal, Global cancer statistics 2018: GLOBOCAN estimates of incidence and mortality worldwide for 36 cancers in 185 countries, CA Cancer J. Clin. 68 (6) (2018) 394–424, https://doi.org/10.3322/caac.21492.

[2] E. Morgan, et al., Global burden of colorectal cancer in 2020 and 2040: incidence and mortality estimates from GLOBOCAN, Gut 72 (2) (2023) 338, https://doi.org/10.1136/gutjnl-2022-327736.

[3] M.S. Hossain et al., Colorectal cancer: a review of carcinogenesis, global epidemiology, current challenges, risk factors, preventive and treatment strategies, Cancers (Basel), 14(7) (2022), doi: 10.3390/cancers14071732.

[4] B. Gustavsson, et al., A review of the evolution of systemic chemotherapy in the management of colorectal cancer, Clin. Colorectal Cancer 14 (1) (2015) 1–10, https://doi.org/10.1016/j.clcc.2014.11.002.

[5] Y.H. Xie, Y.X. Chen, J.Y. Fang, Comprehensive review of targeted therapy for colorectal cancer, Signal Transduct. Target. Ther. 5 (1) (2020) Dec, https://doi.org/10.1038/s41392-020-0116-z.

[6] P. Gogoi, G. Kaur, N.K. Singh, Nanotechnology for colorectal cancer detection and treatment, World J. Gastroenterol. 28 (46) (2022) 6497–6511, https://doi.org/10.3748/wjg.v28.i46.6497.

[7] L. Racca, V. Cauda, Remotely activated nanoparticles for anticancer therapy, Nanomicro Lett., 13(1) (2021), doi: 10.1007/s40820-020-00537-8.

[8] C.H. Wong, K.W. Siah, A.W. Lo, Estimation of clinical trial success rates and related parameters, Biostatistics 20 (2) (2019) 273–286, https://doi.org/10.1093/biostatistics/kxx069.

[9] F. Castro, et al., Advances on colorectal cancer 3D models: the needed translational technology for nanomedicine screening, Adv. Drug Deliv. Rev. 175 (2021), https://doi.org/10.1016/j.addr.2021.06.001.

[10] J. Costa, A. Ahluwalia, Advances and current challenges in intestinal in vitro model engineering: a digest, Front. Bioeng. Biotechnol., 7(JUN) (2019), doi: 10.3389/fbioe.2019.00144.

[11] G.S. Ferreira et al., A standardised framework to identify optimal animal models for efficacy assessment in drug development, PLoS One, 14(6) (2019), doi: 10.1371/journal.pone.0218014.

[12] M.B. Bracken, Why animal studies are often poor predictors of human reactions to exposure, J. R. Soc. Med. 102 (3) (2009) 120–122, https://doi.org/10.1258/jrsm.2008.08k033.

[13] E. Nascimento-Gonçalves, B.A.L. Mendes, R. Silva-Reis, A.I. Faustino-Rocha, A. Gama, P.A. Oliveira, Animal models of colorectal cancer: From spontaneous to genetically engineered models and their applications, Vet. Sci., 8(4) (2021), doi: 10.3390/vetsci8040059.

[14] Í. Neto, J. Rocha, M.M. Gaspar, C.P. Reis, Experimental murine models for colorectal cancer research, Cancers (Basel), 15(9) (2023), doi: 10.3390/cancers15092570.

[15] S.K. Doke, S.C. Dhawale, Alternatives to animal testing: a review, Saudi Pharma. J. 23 (3) (2015) 223–229, https://doi.org/10.1016/j.jsps.2013.11.002.

[16] Y. Wang, R. Kim, S.S. Hinman, B. Zwarycz, S.T. Magness, N.L. Allbritton, Bioengineered systems and designer matrices that recapitulate the intestinal stem cell niche, CMGH, (2018), doi: 10.1016/j.jcmgh.2018.01.008.

[17] T. Shyam Mohan, P. Datta, S. Nesaei, V. Ozbolat, I.T. Ozbolat, 3D coaxial bioprinting: Process mechanisms, bioinks and applications, Prog. Biomed. Eng., 4 (2) (2022), doi: 10.1088/2516-1091/ac631c.

[18] Q. Pi et al., Digitally tunable microfluidic bioprinting of multilayered cannular tissues, Adv. Mater., 30(43) (2018), doi: 10.1002/adma.201706913.

[19] Y. Yu, Y. Zhang, J.A. Martin, I.T. Ozbolat, Evaluation of cell viability and functionality in vessel-like bioprintable cell-laden tubular channels, J. Biomech. Eng., 135(9) (2013), doi: 10.1115/1.4024575.

[20] W. Jia, et al., Direct 3D bioprinting of perfusable vascular constructs using a blend bioink, Biomaterials 106 (2016) 58–68, https://doi.org/10.1016/j.biomaterials.2016.07.038.

[21] S. Maharjan, J.J. He, L. Lv, D. Wang, Y.S. Zhang, Microfluidic coaxial bioprinting of hollow, standalone, and perfusable vascular conduits, Methods Mol. Biol. 2375 (2022) 61–75, https://doi.org/10.1007/978-1-0716-1708-3_6. Humana Press Inc.

[22] D. Wang, et al., Microfluidic bioprinting of tough hydrogel-based vascular conduits for functional blood vessels, Sci. Adv. 8 (2022) 6900, https://doi.org/10.2021/ACE2_HUVSMCs/Image.

[23] G. Rosso, et al., Acoustic waves and smart biomimetic nanoparticles: combination treatment from 2D to 3D colorectal cancer models, Cancer Nanotechnol. 15 (1) (2024), https://doi.org/10.1186/s12645-024-00281-3.

[24] G. Canavese, et al., Nanoparticle-assisted ultrasound: a special focus on sonodynamic therapy against cancer, Chem. Eng. J. 340 (2018) 155–172, https://doi.org/10.1016/j.cej.2018.01.060.

[25] M. Carofiglio et al., Iron-doped zno nanoparticles as multifunctional nanoplatforms for theranostics, Nanomaterials, 11(10) (2021), doi: 10.3390/nano11102628.

[26] M. Conte, M. Carofiglio, G. Rosso, V. Cauda, Lipidic formulations inspired by COVID vaccines as smart coatings to enhance nanoparticle-based cancer therapy, Nanomaterials 13 (15) (2023), https://doi.org/10.3390/nano13152250.

[27] M. Koolpe, M. Dail, E.B. Pasquale, An ephrin mimetic peptide that selectively targets the EphA2 receptor, J. Biol. Chem. 277 (49) (2002) 46974–46979, https://doi.org/10.1074/jbc.M208495200.

[28] L. Racca, et al., Effective combination of biocompatible zinc oxide nanocrystals and high-energy shock waves for the treatment of colorectal cancer, Cancer Nanotechnol. 14 (1) (2023), https://doi.org/10.1186/s12645-023-00195-6.

[29] J. Sun, H. Tan, Alginate-based biomaterials for regenerative medicine applications, Materials 6 (4) (2013) 1285–1309, https://doi.org/10.3390/ma6041285.

[30] E. Axpe, M.L. Oyen, Applications of alginate-based bioinks in 3D bioprinting, Int. J. Mol. Sci. 17 (12) (2016) Dec, https://doi.org/10.3390/ijms17121976.

[31] R. Ahmad Raus, W.M.F. Wan Nawawi, R.R. Nasaruddin, Alginate and alginate composites for biomedical applications, Asian J. Pharm. Sci., 16(3) (2021) 280–306, doi: 10.1016/j.ajps.2020.10.001.

[32] G. Yang, et al., Enzymatically crosslinked gelatin hydrogel promotes the proliferation of adipose tissue-derived stromal cells, PeerJ 4 (2016) e2497.

[33] R. Parenteau-Bareil, R. Gauvin, F. Berthod, Collagen-based biomaterials for tissue engineering applications, Materials 3 (3) (2010) 1863–1887, https://doi.org/10.3390/ma3031863.

[34] C.K. Kuo, P.X. Ma, Maintaining dimensions and mechanical properties of ionically crosslinked alginate hydrogel scaffolds in vitro, J. Biomed. Mater. Res. A 84 (4) (2008) 899–907, https://doi.org/10.1002/jbm.a.31375.
[35] T.R. Keenan, 10.13 - Gelatin, in Polymer Science: A Comprehensive Reference, K. Matyjaszewski and M. Möller, Eds., 2012, pp. 237–247. doi: https://doi.org/10.1016/B978-0-444-53349-4.00265-X.
[36] E. Herrero, E. Martin del Valle, M. Galán, Development of a new technology for the production of microcapsules based in atomization processes, Chem. Eng. J. 117 (2006) 137–142, https://doi.org/10.1016/j.cej.2005.12.022.
[37] M. Brzezińska, G. Szparaga, The effect of sodium alginate concentration on the rheological parameters of spinning solutions, Autex Res. J. (2015), https://doi.org/10.2478/aut-2014-0044.
[38] C. Fan, et al., Viscosity and degradation controlled injectable hydrogel for esophageal endoscopic submucosal dissection, Bioact. Mater. 6 (4) (2021) 1150–1162, https://doi.org/10.1016/j.bioactmat.2020.09.028.
[39] G.M. Pawar, et al., Injectable hydrogels from segmented PEG-bisurea copolymers, Biomacromolecules 13 (12) (2012) 3966–3976, https://doi.org/10.1021/bm301242v.
[40] C.K. Kuo, P.X. Ma, Ionically crosslinked alginate hydrogels as scaffolds for tissue engineering: Part 1. Structure, gelation rate and mechanical properties, Biomaterials 22 (6) (2001) 511–521, https://doi.org/10.1016/S0142-9612(00)00201-5.
[41] M. Blanco-López, A. Marcos García, A. Gonzalez Garcinuño, A. Tabernero, E. Martin del Valle, Exploring the effect of experimental conditions on the synthesis and stability of alginate–gelatin coacervates, Polym. Adv. Technol. 35 (2024) Aug, https://doi.org/10.1002/pat.6554.
[42] G. Yang, et al., Enzymatically crosslinked gelatin hydrogel promotes the proliferation of adipose tissue-derived stromal cells, PeerJ 9 (2016) 2016, https://doi.org/10.7717/peerj.2497.
[43] S. Kawano, M. Kojima, Y. Higuchi, M. Sugimoto, K. Ikeda, N. Sakuyama, S. Takahashi, R. Hayashi, A. Ochiai, N. Saito, Assessment of elasticity of colorectal cancer tissue, clinical utility, pathological and phenotypical relevance, Cancer Sci. 106 (9) (2015) 1232–1239, https://doi.org/10.1111/cas.12720.
[44] C.F. Guimarães, L. Gasperini, A.P. Marques, R.L. Reis, The stiffness of living tissues and its implications for tissue engineering, Nat. Rev. Mater. 5 (5) (2020) 351–370, https://doi.org/10.1038/s41578-019-0169-1.
[45] T. Gregory, P. Benhal, A. Scutte, D. Quashie, K. Harrison, C. Cargill, S. Grandison, M.J. Savitsky, S. Ramakrishnan, J. Ali, Rheological characterization of cell-laden alginate-gelatin hydrogels for 3D biofabrication, J. Mech. Behav. Biomed. Mater. 136 (2022) 105474, https://doi.org/10.1016/j.jmbbm.2022.105474.
[46] M.B. Christensen, K. Oberg, J.C. Wolchok, Tensile properties of the rectal and sigmoid colon: a comparative analysis of human and porcine tissue, Springerplus 4 (1) (2015) Dec, https://doi.org/10.1186/s40064-015-0922-x.
[47] D. Ahmed, et al., Epigenetic and genetic features of 24 colon cancer cell lines, Oncogenesis 2 (2013), https://doi.org/10.1038/oncsis.2013.35.
[48] F. Castro et al., Advances on colorectal cancer 3D models: the needed translational technology for nanomedicine screening, (2021), Elsevier B.V. doi: 10.1016/j.addr.2021.06.001.
[49] M. Carofiglio, M. Laurenti, G.G. Genchi, G. Ciofani, M. Grochowicz, V. Cauda, Ultrasound triggered ZnO-based devices for tunable and multifaceted biomedical applications, Adv. Mater. Interfaces 8 (21) (2021) Nov, https://doi.org/10.1002/admi.202101021.
[50] L. Racca, et al., Zinc oxide nanocrystals and high-energy shock waves: a new synergy for the treatment of cancer cells, Front. Bioeng. Biotechnol. 8 (2020), https://doi.org/10.3389/fbioe.2020.00577.
[51] A. Troia, S. Galati, V. Vighetto, V. Cauda, Piezo/sono-catalytic activity of ZnO micro/nanoparticles for ROS generation as function of ultrasound frequencies and dissolved gases, Ultrason. Sonochem. 97 (2023), https://doi.org/10.1016/j.ultsonch.2023.106470.
[52] B. Dumontel, et al., ZnO nanocrystals shuttled by extracellular vesicles as effective Trojan nano-horses against cancer cells, Nanomedicine 14 (21) (2019) 2815–2833, https://doi.org/10.2217/nnm-2019-0231.
[53] J.W. Rasmussen, E. Martinez, P. Louka, D.G. Wingett, Zinc oxide nanoparticles for selective destruction of tumor cells and potential for drug delivery applications, Expert Opin. Drug Deliv. 7 (9) (2010) 1063–1077, https://doi.org/10.1517/17425247.2010.502560.